

University of Nebraska - Lincoln

DigitalCommons@University of Nebraska - Lincoln

Faculty Publications from Nebraska Center for
Materials and Nanoscience

Materials and Nanoscience, Nebraska Center
for (NCMN)

12-1-1994

NMR and NQR study of the electronic and structural properties of Al-Cu-Fe and Al-Cu-Ru quasicrystals

A. Shastri

Ames Laboratory, U.S. Department of Energy and Department of Physics and Astronomy, Iowa State University, Ames, Iowa

F. Borsa

Ames Laboratory, U.S. Department of Energy and Department of Physics and Astronomy, Iowa State University, Ames, Iowa

D.R. Torgeson

Ames Laboratory, U.S. Department of Energy and Department of Physics and Astronomy, Iowa State University, Ames, Iowa


Jeffrey E. Shield

University of Nebraska - Lincoln, jshield@unl.edu

A.I. Goldman

Ames Laboratory, U.S. Department of Energy and Department of Physics and Astronomy, Iowa State University, Ames, Iowa

Follow this and additional works at: <https://digitalcommons.unl.edu/cmrafacpub>

 Part of the [Nanoscience and Nanotechnology Commons](#)

Shastri, A.; Borsa, F.; Torgeson, D.R.; Shield, Jeffrey E.; and Goldman, A.I., "NMR and NQR study of the electronic and structural properties of Al-Cu-Fe and Al-Cu-Ru quasicrystals" (1994). *Faculty Publications from Nebraska Center for Materials and Nanoscience*. 51.
<https://digitalcommons.unl.edu/cmrafacpub/51>

This Article is brought to you for free and open access by the Materials and Nanoscience, Nebraska Center for (NCMN) at DigitalCommons@University of Nebraska - Lincoln. It has been accepted for inclusion in Faculty Publications from Nebraska Center for Materials and Nanoscience by an authorized administrator of DigitalCommons@University of Nebraska - Lincoln.

NMR and NQR study of the electronic and structural properties of Al-Cu-Fe and Al-Cu-Ru quasicrystals

A. Shastri, F. Borsa,* D. R. Torgeson, J. E. Shield,[†] and A. I. Goldman

Ames Laboratory, U.S. Department of Energy and Department of Physics and Astronomy, Iowa State University, Ames, Iowa 50011

(Received 2 June 1994)

²⁷Al and ^{63,65}Cu NMR measurements are reported for powder samples of stable Al-Cu-Fe and Al-Cu-Ru icosahedral quasicrystals and their crystalline approximants, and for an Al-Pd-Mn single-grain quasicrystal. Furthermore, ²⁷Al NQR spectra at 4.2 K have been observed in the Al-Cu-Fe and Al-Cu-Ru samples. From the quadrupole-perturbed NMR spectra at different magnetic fields, and from the zero-field NQR spectra, a wide distribution of local electric-field gradient (EFG) tensor components and principal-axis-system orientations was found at the Al site. A model EFG calculation based on a 1/1 Al-Cu-Fe approximant was successful in explaining the observed NQR spectra. The average local gradient is largely determined by the *p*-electron wave function at the Al site, while the width of the distribution is due to the lattice contribution to the EFG. Comparison of ⁶³Cu NMR with ²⁷Al NMR shows the EFG distribution at the two sites is similar, but the electronic contribution to the EFG is considerably smaller at the Cu site, in agreement with a more *s*-type wave function of the conduction electrons. The overall spread of EFG values is well reproduced by the calculation based on the approximant. However, the experimental spectra indicate a much larger number of nonequivalent sites when compared with the simulated NQR spectra based on the 1/1 approximant. The short-range, local chemical order is well represented by the approximant, but differences in coordination must be included at intermediate range in the quasicrystal. Measurements of ²⁷Al Knight shift, magnetic susceptibility, and nuclear spin-lattice relaxation time as a function of temperature yield results which indicate a reduction of the density of states at the Fermi level by a factor of 7 or 8 from the value in Al metal, consistent with the notion of a pseudogap for these quasicrystals. No differences in the measured parameters were detected as a function of composition of the quasicrystalline alloys, arguing against a fine structure in the density of states at the Fermi level.

I. INTRODUCTION

Quasicrystals (QCs) are one of the many examples of noncrystalline structures. They possess long-range order but noncrystallographic orientational order.¹ Although important open questions remain, the fundamental structural principles are well understood and elegant descriptions of the quasiperiodicity in terms of higher-dimensional periodic lattices have been given.

One important class of quasicrystals is represented by metallic alloys with icosahedral point-group symmetry (*I* phases). Among these are Al-Cu-Fe and Al-Cu-Ru, which form stable *I* phases over a wide compositional range. The Al-Cu-Fe system may be prepared in either the QC or crystalline approximant (*C*) phase. For these reasons this experimental investigation will focus on these two alloy systems.

The recognition that the related crystalline compounds consist of interpenetrating atomic clusters with icosahedral symmetry motivates cluster-based quasicrystal models, which describe local order over distances of tens of angstroms.¹ One important question in this regard is the location of each atom in the cluster.

Because quasiperiodic systems lack lattice translational symmetry, there is no Brillouin zone in the ordinary sense. This fact brings about the possibility of unusual electronic properties in comparison with those seen in the

periodic and amorphous systems. The mechanism that provides thermal stability for the *I* phase alloys is of particular interest. The *I* phases are Hume-Rothery alloys, and consequently the minimum in the density of states occurs at the Fermi energy.² This minimum, called a pseudogap, lowers the energy of the occupied states and raises the energy of the unoccupied states,² thus enhancing the cohesive energy of the *I* phase.

Nuclear magnetic resonance (NMR) provides a local probe which can be used in principle to obtain information about (1) local atomic environments through the nuclear quadrupole interactions; and (2) local electronic and magnetic structure through the magnetic hyperfine interactions. Furthermore, nuclear spin-lattice relaxation (NSLR) can give information about excitations and fluctuations in the system. Previous NMR studies of quasicrystals have indicated the presence of (1) wide distributions of electric-field gradients consistent with a distribution of local environments,³⁻⁹ (2) vanishingly small Knight shifts;^{4-6,9-12} and (3) long NSLR consistent with very low density of states (DOS) at the Fermi level.^{6,8,9,11,12} In nonmagnetic QC systems, the various NMR parameters were found to be rather insensitive to changes in the stoichiometry of the *I* phase alloys^{6,9,12} and of the structure being *C* or QC.^{7,9,11} In the magnetic *I* phases, *C* and QC phases have exhibited nearly identical static NMR parameters,^{3,5} but many exhibit drastically

different dynamic NMR parameters.¹³ This is because local magnetic moments can give rise to magnetic phases which drastically affect the NMR parameters.

In nonmagnetic QC's, interest remains concerning possible anomalous NMR features occurring at high temperature and their relationship to the existence of a sharp pseudogap at the Fermi level.¹⁴ These high-temperature measurements may give insight into the nature of phason excitations and defect diffusion. In view of this we undertook a detailed and systematic investigation of the NMR parameters in QC and C phases at room temperature and below to provide a frame of reference to which to refer for further work. NMR measurements were performed on both ²⁷Al and ^{63,65}Cu nuclei at different resonance frequencies and temperatures in a series of QC phases, Al_{85-x}Cu_xRu₁₅ with different compositions ($x=15,17,20$); and in Al₆₅Cu₂₃Fe₁₂ in both the QC and the C phases. In addition, measurements in a single-grain Al-Pd-Mn QC are presented here.

The distribution of quadrupole coupling constants in quasicrystals produces line broadening which tends to mask the very small Knight shifts present. Thus only a detailed analysis of spectra at different applied fields, to be described later, allows one to measure the Knight-shift tensor components with some confidence. In the latter stages of our investigation, we were able to detect the ²⁷Al nuclear quadrupole resonance (NQR) spectrum in Al-Cu-Fe and Al-Cu-Ru quasicrystals at 4.2 K.¹⁵ These zero-field NQR measurements give direct access to the distribution of local electric-field gradients, avoiding the complication of powder averages inherent in the NMR measurements in multigrain samples.

In Sec. II we will present the experimental methods, and in Sec. III the ²⁷Al NMR and NQR spectra. From the fit of the quadrupole-perturbed NMR spectra with theoretical NMR line-shape simulations, one can obtain the average quadrupole coupling constant. In addition, more detailed information about the distribution of non-equivalent nuclear sites is obtained from the ²⁷Al NQR spectra. Section III also includes the comparison of line shapes for single-grain and powder samples. In Sec. IV the results for the Knight shifts, the magnetic susceptibility, and the NSLR are presented and discussed in terms of the electronic structure. In Sec. V a summary and the conclusions are given.

II. EXPERIMENTAL DETAILS AND DATA ANALYSIS

A. Samples

Al_{85-x}Cu_xRu₁₅ ($x=15,17,20$) and Al₆₅Cu₂₃Fe₁₂ alloys were prepared by arc-melting appropriate proportions of high-purity (better than 99.9%) metals in an argon atmosphere. To ensure complete mixing, each button was turned over and remelted twice. The buttons were then broken and examined by eye for homogeneous mixing of the metals. They were then remelted into ingots. The ingots were then sealed inside quartz tubes at 10⁻⁴ torr in preparation for heating. The quasicrystalline phases were prepared by heating both the Al-Cu-Ru and the Al-Cu-Fe ingots at 800°C for 23 days. In order to obtain the C

phase of the Al-Cu-Fe system¹⁶⁻¹⁹ one of the QC ingots was further heated at 650°C for 50 h. The final ingots were ground into powders for susceptibility and NMR measurements.

Single-grain and powder samples of the Al₇₀Pd_{2.15}Mn_{8.5} QC were also prepared. The single-grain sample was the same sample used in a previous study.²⁰ It was prepared by first growing single-grain regions in an ingot using the Bridgman technique. A single grain was selected and then cut from the ingot after neutron diffraction was used to determine the single-grain regions. This region was cut to the dimensions 0.1×0.28×0.5 in.³ with twofold axes perpendicular to the two largest faces. X-ray topography was then used to study the two largest surfaces, and the sample was flipped 180° to ensure that both sides were perpendicular to twofold axes. The powder sample was prepared by arc-melt drop casting and was better than 90% face-centered icosahedral (FCI) phase.

Prior to the NMR measurements the QC powder samples were checked with x-ray scans. Typical spectra are shown in Fig. 1(a) where it can be seen that sharp lines appear consistent with the face-centered icosahedral phase. The Al-Cu-Fe sample in the C phase shows peak-broadening asymmetry consistent with the twinned rhombohedral phase.^{16,17}

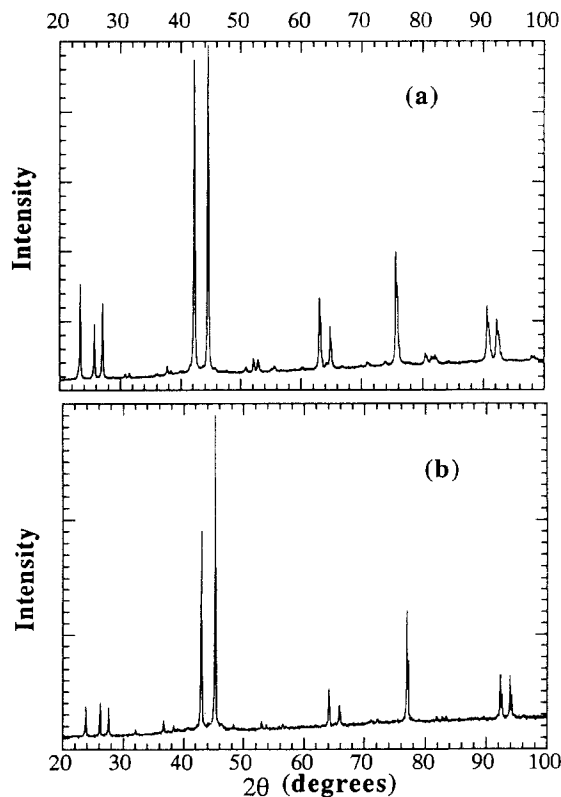


FIG. 1. X-ray diffraction scans for (a) typical Al-Cu-Ru QC sample; the scan is for Al₆₅Cu₁₇Ru₁₅; (b) Al-Cu-Fe sample; the scan is for the Al₆₅Cu₂₃Fe₁₂ QC phase.

B. Magnetic susceptibility

Susceptibility measurements were performed on a superconducting quantum interference device (SQUID) magnetometer using the following procedure. After demagnetizing the external magnetic field to eliminate the residual field, the sample was inserted into the magnetometer and cooled to the lowest temperature of the scan range. A 2-T field was then turned on and the measurements were made as the sample was heated. The sample masses were typically 10 g and the temperature stability was within 0.5%. The magnetometer resolution was better than 10^{-6} emu, with a precision in the magnetic field value of about 1 G. The estimated uncertainty in the experimental atomic susceptibility values is 3% of the measured value.

C. NMR line-shape measurements

The measurements were performed at various resonance frequencies with phase-coherent Fourier transform (FT) pulse spectrometers. The home-built spectrometers use a programmable pulse sequencer, a double-sideband radio-frequency (rf) switch, and a wideband receiver.²¹

Both the ^{27}Al and $^{63,65}\text{Cu}$ nuclei investigated have $I > \frac{1}{2}$ and sizable quadrupole moments. As a result, the NMR spectrum displays a narrower field-dependent central-line ($+\frac{1}{2} \leftrightarrow -\frac{1}{2}$) transition and a field-independent broader line arising from the distribution of satellite ($\pm\frac{5}{2} \leftrightarrow \pm\frac{3}{2}, \pm\frac{3}{2} \leftrightarrow \pm\frac{1}{2}$) transitions. At 8.2 T the full width at half maximum (FWHM) of the central line is 50 kHz for ^{27}Al and roughly 200 kHz for ^{63}Cu (see Fig. 2). The rf field H_1 was about 50 G at these frequencies, allowing one to uniformly irradiate the ^{27}Al central line and about a quarter of the ^{63}Cu central line. Thus the line shape of the central line can be obtained directly by FT of half of the echo signal only for ^{27}Al . In order to obtain the central-line spectrum at low field, where the line is broader, and the spectrum of the satellite distribution, we had to use either frequency-swept or field-swept scans. In

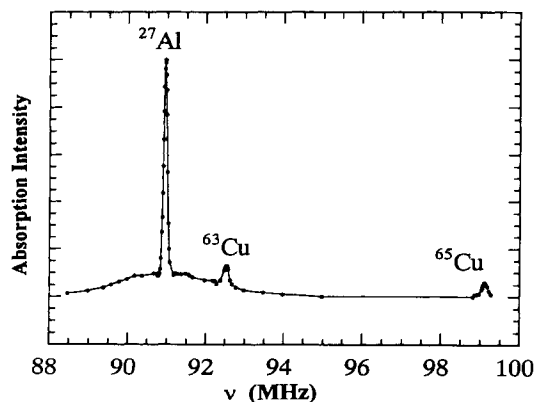


FIG. 2. NMR spectrum of typical Al-Cu-Ru(Fe) sample at 8.2 T and 77 K. $\text{Al}_{65}\text{Cu}_{20}\text{Ru}_{15}$ shows a narrow ^{27}Al central line, a wide ^{27}Al satellite background, and $^{63,65}\text{Cu}$ central-line resonances. The spectrum was obtained by plotting echo height as a function of spectrometer carrier frequencies.

both cases the echo signal was generated by a two-pulse Hahn-echo sequence. For field scans the echo signal was integrated by means of a boxcar integrator and the integrated signal was digitized and stored in a Nicolet 1170 signal averager while the external magnetic field was scanned slowly and continuously. Usually 100–200 scans were sufficient to obtain a good signal-to-noise ratio. For frequency scans the spectrum was obtained point by point by changing the irradiating frequency in steps that varied from 10 kHz in the central lines to 200 kHz in the satellite distribution. The NMR probe was retuned at each point. A silver rf coil was used to avoid spurious $^{63,65}\text{Cu}$ signals, and all calibrations were made by using the ^{27}Al resonance in a saturated aqueous AlCl_3 solution.

D. NQR line-shape measurements

The ^{27}Al NQR measurements were performed with a phase-coherent pulse Fourier-transform spectrometer operating at variable frequency.²¹ The ^{27}Al NQR signal was detected at 4.2 K as an echo signal following a $\pi/2|_{\{x,\bar{x}\}} - \pi/2|_y$ pulse sequence with $\tau_{\pi/2} = 10 \mu\text{s}$ and pulse separation 100 μs . For ^{27}Al ($I = \frac{5}{2}$) one expects two resonance lines.²² The $\pm\frac{3}{2} \leftrightarrow \pm\frac{1}{2}$ transition occurs at $\nu_1 = \nu_Q g(\eta)$, where $\nu_Q \equiv 3eQ|V_{zz}^{\text{tot}}|/20h$, eQ is the nuclear quadrupole moment, and the asymmetry parameter is $\eta \equiv (V_{xx} - V_{yy})/V_{zz}$. The function $g(\eta)$ was tabulated in Ref. 23, and varies from 1 for $\eta=0$ to 1.8 for $\eta=1$. The $\pm\frac{5}{2} \leftrightarrow \pm\frac{3}{2}$ transition occurs at $\nu_2 = 2\nu_Q f(\eta)$, and $f(\eta)$ varies from 1 at $\eta=0$ to 0.88 at $\eta=1$.²³ The functions $f(\eta)$ and $g(\eta)$ are shown in Fig. 3. The echo intensity at the lowest end of the frequency spectrum may have been slightly underestimated as a consequence of the decrease of the power output of the rf power amplifier. The NQR spectrum we report is ascribed to the $\pm\frac{5}{2} \leftrightarrow \pm\frac{3}{2}$ transitions of ^{27}Al , and the average ν_R from NQR agreed well with previous quadrupole-perturbed NMR spectra in Al-Cu-Fe and Al-Cu-Ru.⁹ Due to the extreme width of the NQR spectrum and to the very short $T_2 = 80 \mu\text{s}$, the signal-to-noise ratio was poor even at 4.2 K. In order to

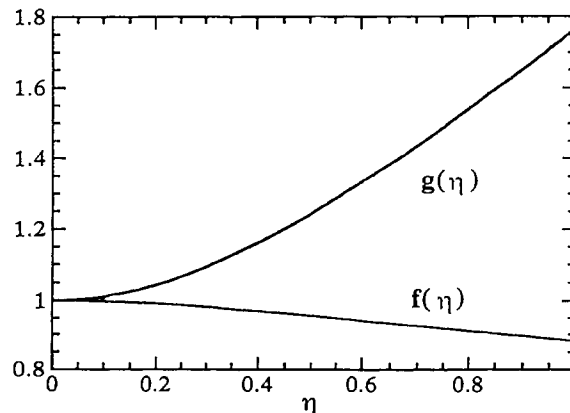


FIG. 3. The functions $g(\eta)$ ($\pm\frac{3}{2} \leftrightarrow \pm\frac{1}{2}$ transition) and $f(\eta)$ ($\pm\frac{5}{2} \leftrightarrow \pm\frac{3}{2}$ transition) over the range $0 \leq \eta \leq 1$, calculated in Ref. 23.

enhance the echo intensity, a weak magnetic field ($H_0 \approx 30$ G) was applied perpendicularly to the sample coil axis by means of Helmholtz coils. The applied field was small enough that it did not affect the shape or width of the NQR spectrum, but was large enough to decouple the nuclear spins, making T_2 longer ($T_2 = 500 \mu\text{s}$).²⁴

E. Nuclear spin-lattice relaxation rates

For quadrupolar nuclei, the recovery of the magnetization following a saturating rf pulse is not generally exponential. In order to extract the correct value for the relaxation transition probability W , one has to know the dominant relaxation mechanism and the theoretical expression for the recovery law for a given initial saturation condition.²⁵ For a magnetic relaxation mechanism, one has for the recovery of the central-line transition for $I = \frac{3}{2}$ (Refs. 25 and 26)

$$\frac{M(\infty) - M(t)}{M(\infty)} = 0.1 \exp(-2W_m t) + 0.9 \exp(-12W_m t), \quad (1a)$$

$$\frac{M(\infty) - M(t)}{M(\infty)} = 0.4 \exp(-2W_m t) + 0.6 \exp(-12W_m t), \quad (1b)$$

and for $I = \frac{5}{2}$

$$\begin{aligned} \frac{M(\infty) - M(t)}{M(\infty)} &= 0.029 \exp(-2W_m t) + 0.178 \exp(-12W_m t) \\ &\quad + 0.794 \exp(-30W_m t), \end{aligned} \quad (2a)$$

$$\begin{aligned} \frac{M(\infty) - M(t)}{M(\infty)} &= 0.257 \exp(-2W_m t) + 0.267 \exp(-12W_m t) \\ &\quad + 0.476 \exp(-30W_m t). \end{aligned} \quad (2b)$$

Here W_m is the $\Delta m = \pm 1$ magnetic-relaxation transition probability. Equations (1a) and (2a) correspond to a "short" saturation sequence. In this case, the saturating comb (a sequence of equally spaced pulses applied to saturate the nuclear magnetization) has a duration τ less than the relaxation time $1/2W_m$. Equations (1b) and (2b) correspond to a "long" sequence, i.e., when $\tau \gg 1/2W_m$. This condition ensures that the populations of the $|m| > \pm \frac{3}{2}$ levels have time to redistribute themselves according to the new thermal equilibrium values.

For a quadrupolar relaxation mechanism two constants, W_1 and W_2 , corresponding to the $\Delta m = \pm 1$ and $\Delta m = \pm 2$ allowed transitions, respectively, have to be considered. In this case the analytical solution for the master equation is possible only for $I = \frac{3}{2}$ while for $I = \frac{5}{2}$ this can be done only in special cases (e.g., $W_1 = W_2$).²⁶

Recovery laws for both purely quadrupolar and purely magnetic relaxation were tested to determine which resulted in better fits to the data. The recovery laws for purely quadrupolar relaxation did not result in adequate fits, while the purely magnetic recovery curves did. As

shown in Figs. 4(a), 4(b), and 4(c) the relaxation data are consistent with Eqs. (1a) and (2a) for purely magnetic relaxation.

The case of ^{63}Cu NSLR requires further details. As shown in Fig. 2, the ^{63}Cu resonance overlaps the ^{27}Al satellite transitions even at the highest field $H = 8.2$ T. In order to derive the correct W_m pertaining to ^{63}Cu NSLR the following procedure was used. Relaxation data were obtained both at the resonance frequency of ^{63}Cu and at the frequency symmetrically located with respect to the ^{27}Al central-line frequency. Taking the difference of the two signals the recovery of the ^{63}Cu magnetization was obtained. The corrected and uncorrected W_m values were found to differ by only 10%, within the uncertainty

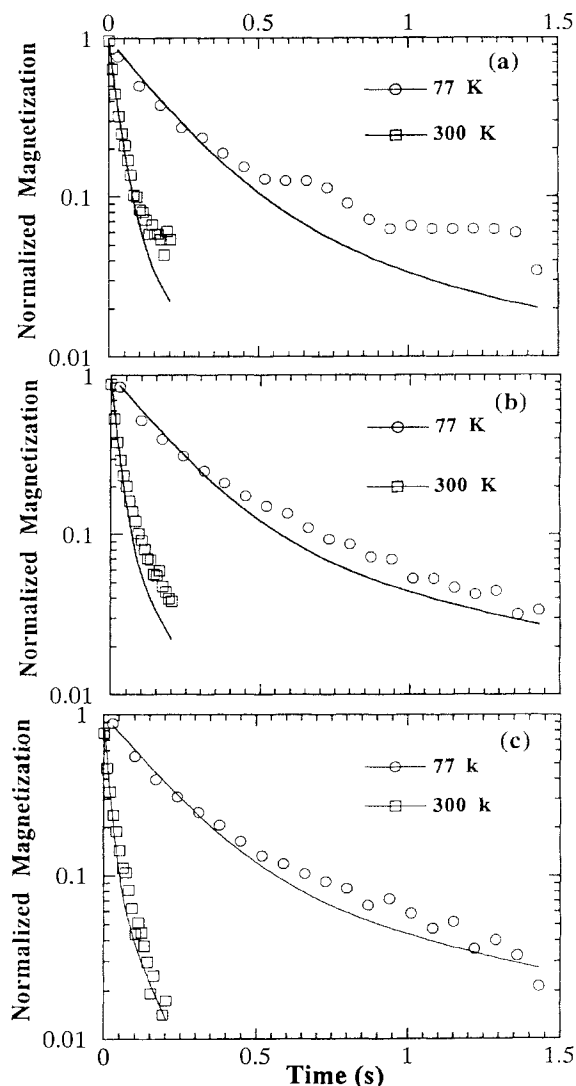


FIG. 4. Semilog plot of the recovery of the normalized nuclear magnetization $[M(\infty) - M(t)]/M(\infty)$ following a "short" saturating rf pulse sequence in $\text{Al}_{65}\text{Cu}_{20}\text{Ru}_{15}$ at 8.2 T and at two different temperatures: (a) ^{27}Al central-line relaxation; (b) ^{63}Cu central-line relaxation; (c) ^{65}Cu central-line relaxation. The full solid curves are theoretical fits by using Eqs. (1a) and (2a) for ^{27}Al and $^{63,65}\text{Cu}$, respectively. The values of W_m obtained from the fits are listed in Table II below.

of the measurements, indicating that the effect of overlap of ^{63}Cu is negligible and can be disregarded.

F. Computer simulation of the ^{27}Al NMR spectrum

A NMR line-shape simulation program was used to generate simulated powder patterns. NMR line-shape simulations have been discussed by many authors,²⁷ and applications to quasicrystalline materials have been reported.^{3,8} The intent of such investigations is to compare simulated spectra with data, modifying simulation parameters until one gets a reasonable fit to the data.

In what follows, the nuclear energy levels, the simulation procedure, and the nature of the distributions used in the simulation will be discussed. When a nucleus of spin $I > \frac{1}{2}$ is placed in a static magnetic field \mathbf{H}_0 and is in a noncubic environment, the total Hamiltonian may be written $\mathcal{H} = \mathcal{H}_0 + \mathcal{H}_{\text{quad}} + \mathcal{H}_{\text{mag}}$, where \mathcal{H}_0 arises from the coupling of the nuclear moment I with the static field \mathbf{H}_0 , $\mathcal{H}_{\text{quad}}$ from the coupling of the nuclear quadrupole moment and the local electric-field gradient (EFG) at the nuclear site, and \mathcal{H}_{mag} from hyperfine interactions of the electronic and nuclear moments. Because the quadrupole and magnetic hyperfine interactions are described by tensor quantities, energy eigenvalues will depend on the orientations of the static magnetic field \mathbf{H}_0 with respect to the principal-axis systems (PAS's) of the electric-field gradient and magnetic hyperfine (MH) interaction tensors. Since both EFG PAS and MH PAS are determined by the symmetry at the nuclear site, we assume that they

are the same, and we call this *the* PAS. This results in great simplification of the problem. In addition, for the case where $\mathcal{H}_0 \gg \mathcal{H}_{\text{quad}}, \mathcal{H}_{\text{mag}}$ the frequencies $\nu = \nu_0 + \nu_{\text{quad}} + \nu_{\text{mag}}$ of the $\Delta m = \pm 1$ transitions can be expressed in terms of the PAS tensor components V_{xx}, V_{yy}, V_{zz} and K_x, K_y, K_z of the EFG and MH tensors, respectively, and the Euler angles θ and ϕ between the PAS and the \mathbf{H}_0 direction.

If one assumes that the EFG at the nuclear site is due solely to charges outside the nucleus, Laplace's equation holds and $V_{xx} + V_{yy} + V_{zz} = 0$. This reduces the number of independent components from three to two, and one may define two independent quantities $\eta \equiv (V_{xx} - V_{yy})/V_{zz}$ and $\epsilon q \equiv V_{zz}$. The zz component is usually written in terms of the quadrupole frequency $\nu_q = 3e^2qQ/2I(2I-1)h$. For the MH tensor quantities, K_x, K_y, K_z are all independent, but it is convenient to write the transition frequencies in terms of the MH quantities

$$K_{\text{iso}} \equiv \frac{1}{3}(K_x + K_y + K_z), \quad \epsilon \equiv \frac{K_y - K_x}{K_{\text{an}}},$$

$$K_{\text{an}} \equiv K_z - K_{\text{iso}}.$$

The expressions for the frequency terms are given below to second order:

$$\begin{aligned} \nu(m, \eta, \nu_Q, K_{\text{iso}}, \epsilon, K_{\text{an}}, \theta, \phi) = & \nu_0 + \nu_{\text{quad}}(m, \eta, \nu_Q, \theta, \phi) \\ & + \nu_{\text{mag}}(m, K_{\text{iso}}, \epsilon, K_{\text{an}}, \theta, \phi), \end{aligned}$$

where

$$\nu_0 = -\gamma H_0, \quad (3)$$

$$\nu_{\text{mag}} = \nu_0 \left\{ K_{\text{iso}} + \frac{K_{\text{an}}}{2}(3 \cos^2 \theta - 1) - \frac{\epsilon K_{\text{an}}}{2} \sin^2 \theta \cos 2\phi \right\}, \quad (4a)$$

$$\begin{aligned} \nu_{\text{quad}} = & -\frac{\nu_Q}{2} \left(m - \frac{1}{2} \right) (3 \cos^2 \theta - 1 - \eta \cos 2\phi \sin^2 \theta) \\ & + \frac{\nu_Q^2}{12\nu_0} \left\{ \frac{3}{2} \sin^2 \theta [(A+B) \cos^2 \theta - B] + \eta \cos 2\phi \sin^2 \theta [(A+B) \cos^2 \theta + B] \right. \\ & \left. + \frac{\eta^2}{6} [A - (A+4B) \cos^2 \theta - (A+B) \cos^2 2\phi (\cos^2 \theta - 1)^2] \right\}, \end{aligned} \quad (4b)$$

where

$$A = 24m(m-1) - 4I(I+1) + 9$$

and

$$B = [6m(m-1) - 2I(I+1) + 3]/4. \quad (27)$$

For cases of nonaxial symmetry there are no analytic solutions for NMR powder patterns, and one must turn to numerical methods. The method used here is described in greater detail in Ref. 27 and is briefly summarized below.

First, one must know whether frequency- or field-scan

data are to be simulated. In what follows, it will be assumed that a frequency scan is to be simulated. The methods for field-scan simulation are similar. Second, if ν_c represents the rf carrier frequency, one must specify the beginning, ending, and increment frequencies of the scan: $\nu_c = \nu_1, \nu_2$, and $\Delta\nu$. Third, at each ν_c the resonance condition must be tested. If

$$|\nu_c - \nu(m, \eta, \nu_Q, K_{\text{iso}}, \epsilon, K_{\text{an}}, \theta, \phi)| < \Delta\nu$$

the resonance condition is met. Physically this would correspond to the carrier frequency being within $\Delta\nu$ of the resonance frequency. Fourth, at resonance the rate of

the dipole transition $m \leftrightarrow m - 1$ is proportional to

$$|\langle m - 1 | I_- | m \rangle|^2 = I(I + 1) - m(m - 1).$$

The simulated NMR spectrum in this case consists of a single δ function with amplitude $I(I + 1) - m(m - 1)$ located at the frequency of the $m \leftrightarrow m - 1$ transitions, assuming it is within the range $\nu_c = \nu_1, \nu_2$. The spectrum that results when all of the $2I + 1$ $m \leftrightarrow m - 1$ transitions are combined will be designated

$$P_1(\nu_c; \eta, \nu_Q, K_{\text{iso}}, \epsilon, K_{\text{an}}, \theta, \phi).$$

Up to this point, the simulation has included no distributions. To simulate NMR spectral data, one must include distributions of ν_Q , η , K_{iso} , ϵ , and K_{an} over nonequivalent sites and, for powders, the random distribution of the grains. For single grains, we have considered the possibility of having nonequivalent nuclear sites, each with different values of the tensor components and different orientation of the PAS. If one assumes

$$P_1(\nu_c; \eta, \nu_Q, K_{\text{iso}}, \epsilon, K_{\text{an}}, \theta, \phi)$$

is normalized to an area of 1, one may define the composite spectrum $P_2(\nu_c)$ as

$$P_2(\nu_c) = \sum_{\text{all}} f(\eta, \nu_Q, K_{\text{iso}}, \epsilon, K_{\text{an}}, \theta, \phi) \times P_1(\nu_c; \eta, \nu_Q, K_{\text{iso}}, \epsilon, K_{\text{an}}, \theta, \phi), \quad (5)$$

where f is the product of all the normalized distribution functions for each variable. If the sample is in the form of a single grain, the sum over θ and ϕ results from the orientations of the PAS in nonequivalent sites. In this case there is a finite number of discrete θ and ϕ values. Therefore not all solid-angle directions will contribute, and the simulated composite pattern has angular dependence. In principle, the simulated spectra should be convoluted with the dipolar broadening. However, since this source of broadening contributes only a few kHz to the width of the line, and since the distribution of quadrupole coupling frequencies is on the order of MHz, the correction is negligible.

III. QUADRUPOLE INTERACTIONS AND STRUCTURAL PROPERTIES

A. ^{27}Al NMR line shape in Al-Cu-Fe and Al-Cu-Ru powders

Since the local environments of atoms in quasicrystals are not as yet well characterized, many questions remain open concerning the presence of nonequivalent atomic sites. NMR line simulations can give insight into the local distributions of nonequivalent sites^{3,8} by allowing one to test the effects of these distributions on simulated NMR line spectra. From Eq. (5) one sees that the line shape depends upon parameters characterizing the EFG and MH tensors, and on the local orientation of the PAS of the tensors with respect to the static magnetic field H_0 . Previous simulations of quasicrystal NMR powder lines gave evidence for distributions of the quadrupole tensor

parameters ν_Q and η in Al-Mn (Ref. 3) and Al-Cu-Fe,⁸ though no simulation has successfully reproduced spectra at different magnetic fields with the same choice of parameters.⁸

We used the NMR line-shape simulation program described in Sec. II to show that we can find parameters that result in simulations that fit the experimental line shapes at three field strengths equally well. The absence of powder pattern singularities suggests that wide distributions of the Hamiltonian parameters η , ν_Q , K_{iso} , ϵ , and K_{an} are involved. As will be discussed in the next section, the anisotropic Knight shift is small as can be deduced from the field dependence of the central-line width. We therefore assumed ϵ and K_{an} to be zero, thus reducing the independent parameters to η , ν_Q , and K_{iso} . By trial and error, we found that a quasicontinuous, Gaussian distribution of ν_Q with the following characteristics showed good agreement with spectral data at three field values (Fig. 5): the second moment was $\sigma = \overline{\nu_Q}/3$, where $\overline{\nu_Q}$ is the mean value of ν_Q ; the distribution was taken to be zero outside the upper and lower limits $\overline{\nu_Q} \pm 5\sigma$; there were 60 discrete values of ν_Q equally spaced over the range 10σ of the Gaussian distribution. The distribution of η values was taken to be uniform, and to reduce the number of loops required in the simulation program only the η values 0, 0.1, 0.2, . . . , 1.0 were used. It was found that composite powder patterns with uniform distribution of $\eta = 0, 0.1, . . . , 0.5$ worked slightly better than simulations for $\eta = 0.5, 0.6, . . . , 1.0$.

Having found good agreement between simulations and data when the above distributions were used, we used the NMR line simulations to extract $\overline{\nu_Q}$ and K_{iso} . A library of simulations at 12 and 24 MHz and 8.2 T for different values of $\overline{\nu_Q}$ was compiled. These simulations were then compared to spectra to determine a $\overline{\nu_Q}$ that worked at all fields. To obtain the isotropic Knight shift K_{iso} using the NMR line simulations, we made two successive approximations where, as a first approximation, K_{iso} was set equal to zero. The simulation for the Al central line was then generated for a static field of 8.2 T, and the simulation was compared to Al FT spectra at 8.2 T. By shifting the simulation $\Delta\nu$ until it lay upon the data peak, we obtained for the second approximation the value $K_{\text{iso}} = \Delta\nu/\nu$, where ν is the center of the data peak. The values of $\overline{\nu_Q}$ and K_{iso} for Al-Cu-Fe and Al-Cu-Ru are given in Table I.

B. ^{27}Al NMR line shape in a single-grain Al-Pd-Mn QC

In crystalline materials, NMR spectra show angular-dependent resonance lines that allow a unique determination of the MH and EFG tensor components. In a single-grain quasicrystal one does not know *a priori* whether the long-range positional order of the QC is going to generate an angular dependence of the NMR spectrum. An angular dependence is expected only if there is a local orientation of the principal-axis systems common to a large fraction of Al sites of the single grain.

The Al-Pd-Mn system is the first QC system in which single grains have been large enough to perform NMR.

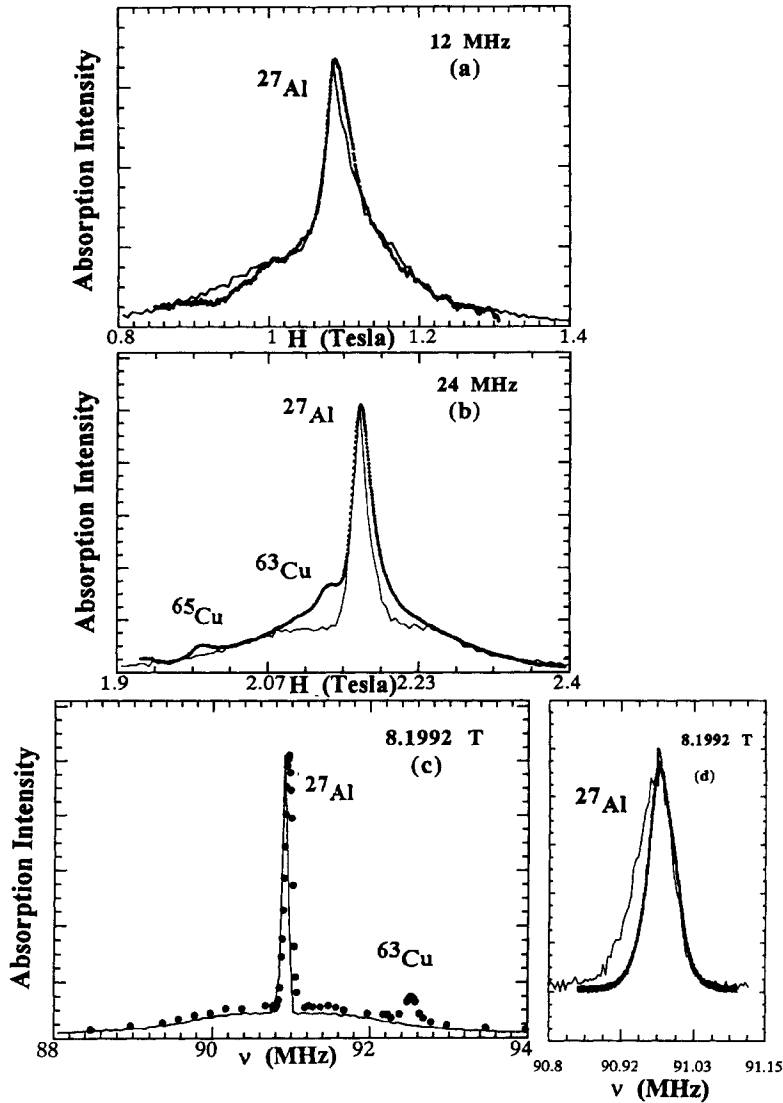


FIG. 5. Data and simulation for ^{27}Al NMR line in $\text{Al}_{65}\text{Cu}_{20}\text{Ru}_{15}$ at 77 K at three different resonance conditions. The heavy line is the data; the light line is the simulation. The parameters used in the simulation are $\overline{\nu_Q} = 2.2$ MHz; $\sigma = \overline{\nu_Q}/3$; $\eta = 0, 0.1, 0.2, \dots, 0.5$. (a) Field scan at 12 MHz; (b) field scan at 24 MHz; (c) frequency scan at 8.2 T; (d) comparison of central-line FT spectrum with simulation.

We oriented the twofold axis of our sample at three different angles α with respect to the static field \mathbf{H}_0 : 0° , 45° , and 90° , and for each orientation the NMR spectrum was taken. No change with α was observed in the central line at 8.2 T [Fig. 6(a)], nor in the satellites at 24 MHz [Fig. 6(b)]. Furthermore, we compared in Fig. 7 the Al-Pd-Mn single-grain spectrum with a powder of nominally the same stoichiometry. The two spectra are nearly identical with only small differences which we attribute to differences in the sample preparation techniques, and to the presence of trace impurity phases in the Al-Pd-Mn powder sample. Because the single-grain NMR spectrum has no angular dependence and is nearly identical to the powder spectrum, we concluded the local EFG tensor has distributions in both the magnitudes of its components and the orientations of its PAS's. In order to verify the extent to which our results are indicative of a distribution of local site symmetries, we show in Fig. 8 the simulated spectra at different angles for the case in which the PAS of the EFG tensor is unique, although we allow for a distribution of magnitudes of the EFG tensor components.

The simulations were performed for the parameters $\nu_Q = 2.1$ MHz; ν_Q Gaussian distribution second moment $\sigma = \nu_Q/3$; asymmetry parameter $\eta = 0$. Figure 8 shows that the shift of the satellites due to the change of angle between the unique PAS and the external magnetic field should be measurable even in the presence of a wide distribution of ν_Q values. The angular independence implies the existence of a large number of local PAS's within the single grain. The data presented point to the conclusion that the distribution of local environments in the single

TABLE I. Values of the parameters $\overline{\nu_Q}$ and K_{iso} .

Sample	$\overline{\nu_Q}$ (MHz)	K_{iso} (%)
$\text{Al}_{70}\text{Cu}_{15}\text{Ru}_{15}$	2.1 ± 0.1	0.026 ± 0.004
$\text{Al}_{68}\text{Cu}_{17}\text{Ru}_{15}$	2.1 ± 0.1	0.024 ± 0.004
$\text{Al}_{65}\text{Cu}_{20}\text{Ru}_{15}$	2.2 ± 0.1	0.024 ± 0.004
Al-Cu-FeC	1.9 ± 0.1	0.016 ± 0.004
Al-Cu-Fe QC	1.8 ± 0.1	0.016 ± 0.004

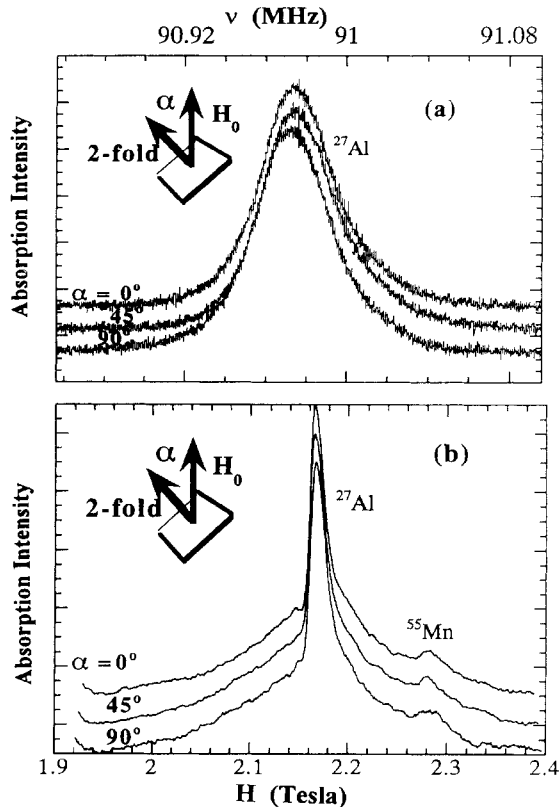


FIG. 6. ^{27}Al NMR line in $\text{Al}_{70}\text{Pd}_{21.5}\text{Mn}_{8.5}$ in a single grain at 77 K for $\alpha=0^\circ$, 45° , and 90° . (a) Central lines at 8.2 T from FT of half echo; (b) satellites and central line at 24 MHz obtained by field scanning.

grain is characterized by a quasicontinuous distribution of PAS orientations and a wide distribution of ν_Q values.

C. ^{27}Al NQR spectra in Al-Cu-Fe and Al-Cu-Ru powders

The ^{27}Al NQR spectra in Al-Cu-Fe and Al-Cu-Ru quasicrystalline powders are shown in Fig. 9. The aver-

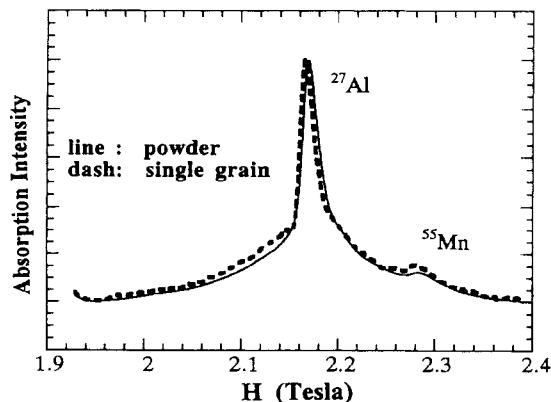


FIG. 7. ^{27}Al NMR line in $\text{Al}_{70}\text{Pd}_{21.5}\text{Mn}_{8.5}$ in a single grain at orientation $\alpha=0^\circ$ compared with powder of nominally the same composition at 77 K. Data were obtained by field scanning at 24 MHz.

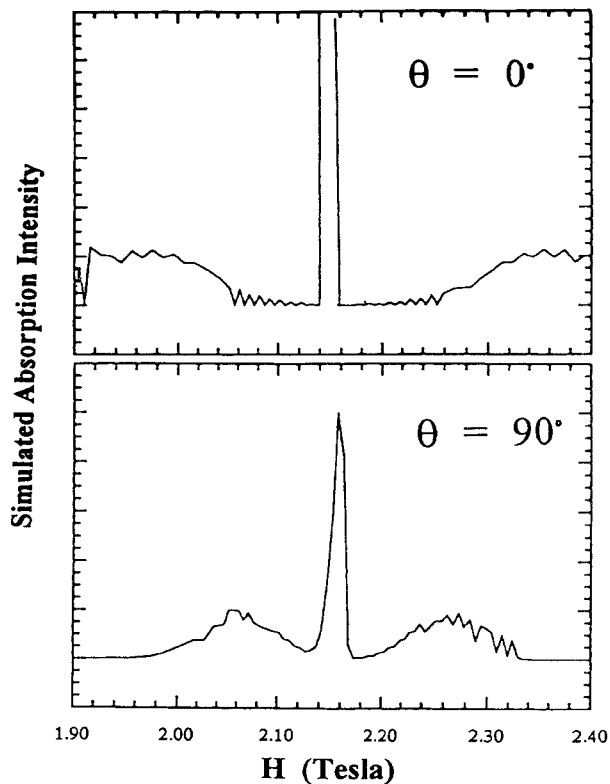


FIG. 8. Simulation for estimating shift in the ^{27}Al central line and satellites in the Al-Pd-Mn single-grain QC. Parameters used in the simulation are $\overline{\nu_Q}=2.1$ MHz, $\sigma=\overline{\nu_Q}/3$, asymmetry parameter values $\eta=0$, and a single PAS. The simulated spectrum is a field scan at 24 MHz for $\theta=0^\circ$ and 90° , where θ is the angle between the z axis and the external field \mathbf{H}_0 . (Note: the coarseness of the discrete frequency steps in the simulation results in the somewhat jagged character of the simulation.)

age NQR resonance frequency $\overline{\nu_R}$ is approximated 4 MHz, which is in agreement with the NMR results if the NQR line originates from the $\pm\frac{5}{2}\leftrightarrow\pm\frac{3}{2}$ transition. In fact, the NQR resonance frequency for this transition is $\nu_R=2\nu_Q f(\eta)$, and since, as shown in Fig. 3, $f(\eta)$ varies by 10% as η changes from 0 to 1, one expects $\nu_R\approx 2\overline{\nu_Q}=4$ MHz, in agreement with the average $\nu_Q\approx 2$ MHz derived from the NMR line-shape simulations for both Al-Cu-Ru and Al-Cu-Fe.

We now compare the width of the distribution of ν_Q from the NQR and NMR data. As discussed previously, we found a Gaussian distribution of ν_Q with second moment $\sigma\approx\overline{\nu_Q}/3$ worked well in simulating the NMR spectrum. From the ^{27}Al NQR spectra of the $\pm\frac{5}{2}\leftrightarrow\pm\frac{3}{2}$ line (Fig. 9), the intensity $I(\nu_R)$ of which gives the distribution of quadrupole resonance frequencies ν_R , one can experimentally determine the second moment σ of the distribution of quadrupole interactions $2\sigma=\sqrt{\overline{\nu_R^2}-\overline{\nu_R}^2}$. We find $\sigma\approx\overline{\nu_Q}/4$ in the case of both Al-Cu-Fe and Al-Cu-Ru. The two values are in qualitative agreement, but the NQR spectrum gives a much more direct and precise indication of the distribution of quadrupole interactions, including an asymmetry of the distribution which is not

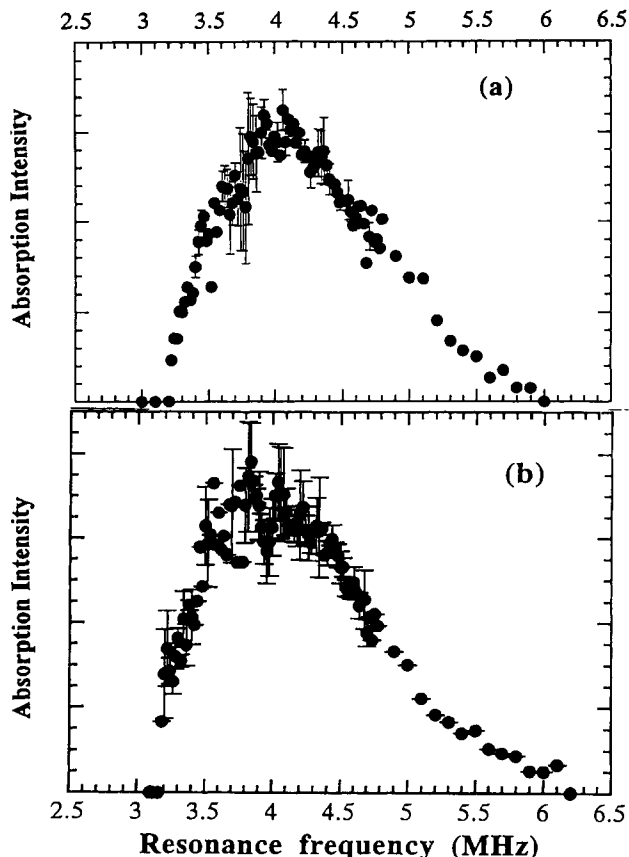


FIG. 9. ^{27}Al NQR spectra for two quasicrystals (a) $\text{Al}_{70}\text{Cu}_{15}\text{Ru}_{15}$ and (b) $\text{Al}_{65}\text{Cu}_{23}\text{Fe}_{12}$ at 4.2 K. Vertical axes were rescaled by ν_R to correct for the Boltzmann distribution.

possible to measure through NMR line-shape simulations.

D. Quadrupole interactions and local symmetry at the Al sites

The quadrupole interactions (QI's) are a sensitive probe of the local symmetry around a given nucleus. The wide distribution of ν_Q values found for the ^{27}Al is a highly relevant result which gives strong evidence for a multiplicity of nonequivalent sites in quasicrystals. Because the width and shape of the NMR line were identical for powder samples and for single-grain samples, we concluded that the distribution of magnitude and orientation of the local EFG tensor is the dominant effect over powder distribution effects. This is confirmed by the strikingly broad and asymmetric NQR spectra, which are a direct measure of the EFG tensor distributions over all nuclear sites in the sample.

A distribution in the local EFG tensor can arise in principle from strain effects and/or from impurities. However, there are two compelling arguments which rule out the possibility that defects are the cause for the distribution of QI's in quasicrystals. The observed linewidth and shape do not change within experimental resolution for samples with different thermal treatment and for different methods of preparation. Furthermore, a comparison with known cases where quadrupole broadening

of the NQR and/or NMR line is due to defects shows that the broadening, even in the worst cases, is always a small fraction of the average $\overline{\nu_Q}$ for a non-cubic site, much smaller than what is found here for ^{27}Al NMR.

Consider the case of zero-field NQR experiments which directly give $\overline{\nu_Q}$ and σ (defined here as the half width at half maximum of the NQR $\pm\frac{3}{2}\leftrightarrow\pm\frac{1}{2}$ line). This ratio is $\sigma/\overline{\nu_Q}\approx\frac{1}{5}$ for the case of ^{27}Al NQR in the quasicrystals studied here. In indium metal one has²⁸ $\overline{\nu_Q}=1.88$ MHz with $\sigma\approx 30$ kHz, and in rhenium metal, which has strong QI's and in which it is difficult to obtain a powder sample free of strains and impurities, one has²⁴ (for the isotope ^{187}Re) $\overline{\nu_Q}=39$ MHz and $\sigma=1.5$ MHz. Therefore $\sigma/\overline{\nu_Q}\approx\frac{1}{63}$ for indium and $\approx\frac{1}{26}$ for rhenium. Another enlightening comparison can be made with recent NQR results in high- T_c superconductors which are known to be poor metals and highly disordered systems. From ^{63}Cu NQR in $\text{YBa}_2(\text{Cu}_{1-x}\text{M}_x)_3\text{O}_7$ doped with different amounts of $M=\text{Zn}$ and Ni one has²⁹ for the case of no doping $\overline{\nu_Q}=31.5$ MHz and $\sigma\approx 100$ kHz giving $\sigma/\overline{\nu_Q}\approx\frac{1}{300}$, and for the doped samples a maximum of $\sigma\approx 400$ kHz giving $\sigma/\overline{\nu_Q}\approx\frac{1}{80}$. Finally ^{139}La NQR measurements³⁰ in La_2CuO_4 doped with Sr yield $\overline{\nu_Q}=6$ MHz and $\sigma\approx 150$ kHz, resulting in $\sigma/\overline{\nu_Q}\approx\frac{1}{40}$. A more direct comparison may be made with the results of ^{27}Al $\pm\frac{5}{2}\leftrightarrow\pm\frac{3}{2}$ NQR transition measurements in both $\text{LaAl}_2:\text{Gd}$ (Ref. 31) and UM_2Al_3 ($M=\text{Ni},\text{Pd}$),³² where the zero-field NQR spectra are centered at about 1.5 MHz with a 20-kHz full width. Therefore it seems clear that the large breadth of the observed ^{27}Al NQR spectra in Al-Cu-Ru and Al-Cu-Fe cannot be attributed simply to the presence of defects in the structure, but rather is a signature of a multiplicity of nonequivalent sites.

One must then account for the broad distribution of interaction strengths in terms of a distribution of nonequivalent sites. The exact calculation of the EFG tensor in metals is quite difficult since it requires the knowledge of both the atomic positions and the wave function of the conduction electrons. Furthermore, some uncertainty remains associated with the shielding effect of the closed-shell core electrons, which is normally taken into account by multiplying the EFG due to external charges by the Sternheimer antishielding factor $(1-\gamma_\infty)$. We present in what follows a simple EFG model calculation which accounts for the experimental observations.

By referring to the greatest component V_{zz} of the EFG tensor in the PAS one can write for metals³³

$$V_{zz}^{\text{tot}} = V_{zz}^{\text{latt}}(1-\gamma_\infty) + V_{zz}^{\text{el}}, \quad (6)$$

where the first term is due to the external ionic charges and the second term is the contribution of the conduction electrons. The latter contribution is normally larger than the first one. A systematic review of the EFG in simple metals has led to the conclusion that in the majority of metals the conduction-electron contribution to the EFG tensor is about three times larger than the lattice contribution and of opposite sign.^{33,34}

The lattice contribution to the total EFG at the Al site [see Eq. (6)] can be calculated accurately if one knows the

location of the Al, Cu, and Ru(Fe) ions and the effective valence of the ions.^{22,35} We have performed an EFG lattice calculation by using a crystalline approximant structure hypothesized for the Al-Cu-Fe and Al-Cu-Ru systems.³⁶ The preliminary structural model is for a $\text{Al}_{80}\text{Cu}_{32}\text{Fe}_{16}$ 1/1 approximant, which has a lattice parameter $a = 12.30$ Å. The valence assignment is somewhat difficult in these alloys due to the poor metallic character of quasicrystals. Thus we have performed the calculation assuming Al^{3+} and Cu^+ as normally found in metals, and three different possible valences for the Fe(Ru) ion: 1+, 2+, 3+. The calculation was performed using the expression for the EFG tensor components^{22,35}

$$V_{ij}^{\text{latt}} = \sum_k \frac{eZ_k}{r_k^3} \left[\frac{3x_i x_j}{r_k^2} - \delta_{ij} \right], \quad (7)$$

where $x_{i=1,2,3}$ are the x , y , and z components of the displacement vector between the Al nucleus at which the EFG is to be calculated and the ions of the lattice with charge Z_k . The calculation was carried out only for lattice ions that satisfy the condition $r/a < 1$, restricting the calculation to roughly the first five nearest-neighbor coordination shells. The EFG tensor was then diagonalized to determine the principal-axis values V_{xx}^{latt} , V_{yy}^{latt} , and V_{zz}^{latt} defined by

$$|V_{zz}^{\text{latt}}| \geq |V_{yy}^{\text{latt}}| \geq |V_{xx}^{\text{latt}}|.$$

The Euler angle θ between the z axis of the crystal coordinates and the z axis of the EFG principal-axis system was also calculated. The distribution of $|V_{zz}|$, η , and θ for different combinations of Al, Cu, and Ru(Fe) ion charges are given in Figs. 10, 11, and 12, respectively. Since successive nearest-neighbor shell contributions fall off as $1/r$, the contribution of the fifth shell was roughly 15% of $500e/a^3$, the contribution due to the first coordination shell. The bin width in the V_{zz}^{latt} histogram (Fig. 10) reflects the uncertainty in the EFG calculation.

Two conclusions can be drawn by inspection of the results in Figs. 10–12. The first one is that the decoration of the clusters used in the approximant involves a multiplicity of nonequivalent sites which give rise to a wide distribution of the EFG components, $|V_{zz}^{\text{latt}}|$ and η , and the PAS orientation θ . The second conclusion is that the choice for the valence of the transition-metal ion affects the details of the distribution of $|V_{zz}^{\text{latt}}|$, η , and θ , but not the overall spread of values.

In order to construct a simulated NQR spectrum for comparison with the experiments, we made the following assumptions: the electronic contribution V_{zz}^{el} in Eq. (6) is opposite in sign to the lattice contribution, and it does not vary appreciably in magnitude over the various Al sites. Furthermore, we assume the asymmetry parameter η of the total EFG is given by the distribution of ionic charges around each Al site and is thus given by the results in Fig. 11.

Based on the above assumptions, we write for the ²⁷Al quadrupole resonance frequency

$$\nu_R = 2\nu_Q f(\eta) = \frac{3eQ}{10h} (|V_{zz}^{\text{el}}| - |V_{zz}^{\text{latt}}|(1 - \gamma_\infty)) f(\eta). \quad (8)$$

We use the values $Q = 0.14 \times 10^{-24}$ cm², $(1 - \gamma_\infty) = 3.3$,³⁵ the calculated values of V_{zz}^{latt} and η for the valence assignment Al^{3+} , Cu^+ , Fe(Ru)^+ (Figs. 10 and 11), and the function $f(\eta)$ in Fig. 3, to obtain the histogram for the NQR spectrum, which is superimposed on the experimental Al-Cu-Ru NQR spectrum as shown in Fig. 13. The value of $V_{zz}^{\text{el}} = 1.77 \times 10^{15}$ esu cm⁻³ was chosen in order to obtain an average ν_R from the histogram which is the same as the experimental value.

The semiempirical value $V_{zz}^{\text{el}} = 1.77 \times 10^{15}$ esu cm⁻³ is of the order of magnitude expected for the electric-field gradient generated by a $3p$ wave at the Al site. In fact,

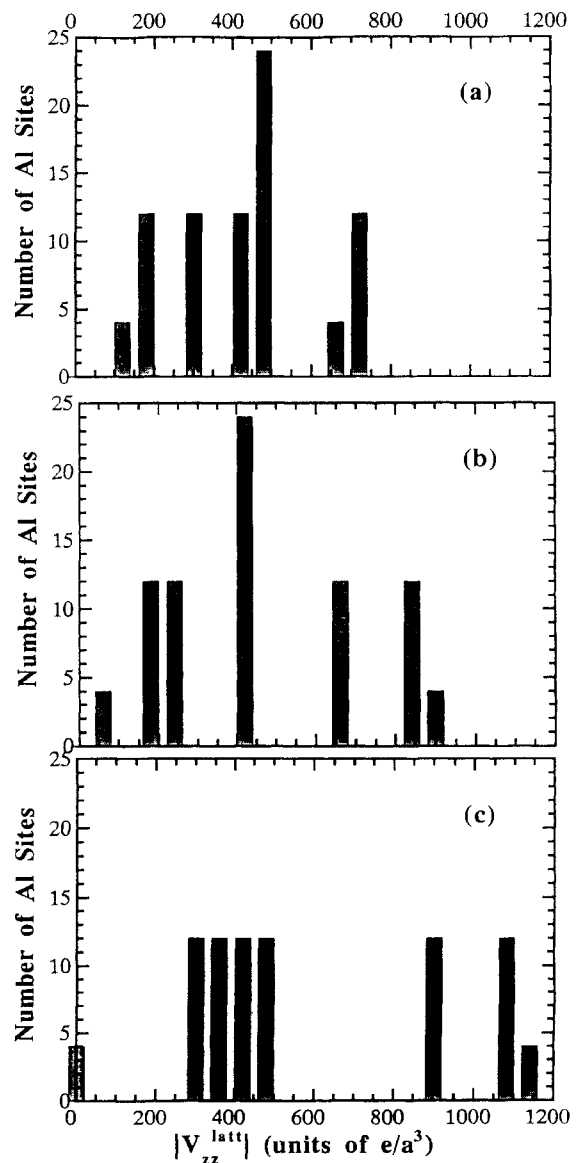


FIG. 10. Distribution of $|V_{zz}|$ EFG values for the aluminum sites, in units of e/a^3 , for different net charges on the Al, Cu, and Ru(Fe) ions, respectively: (a) 3,1,1; (b) 3,1,2; (c) 3,1,3. The bin width is $60e/a^3$.

for a single $3p$ electron in an atom one has²³

$$V_{zz}^{\text{el}} = \frac{4e}{5} \left\langle \frac{1}{r^3} \right\rangle. \quad (9)$$

By using $\langle 1/r^3 \rangle = 1.28/a_0^3$ ($a_0 = 0.529 \text{ \AA}$) as obtained from the hyperfine structure of optical spectra of Al neutral atoms²³ one has $V_{zz}^{\text{el}} = 3.3 \times 10^{15} \text{ esu cm}^{-3}$. It is encouraging that the apparent spatial localization of the Al $3p$ electrons is consistent with the poor metallic character of these quasicrystals.

We emphasize the main point of the above calculation: the model assumes that the total electric-field gradient at a nuclear site is determined primarily by the electronic contribution, and that the width of the NQR spectrum is determined by the distribution of V_{zz}^{latt} through the distribution of local environments. This picture is supported by the fact that the widths of the simulated and experi-

mental NQR spectra of Fig. 13 are similar. However, the structural model of Cockayne *et al.*,³⁶ which we applied to the above calculation, does not result in a continuous distribution of ν_R values. Since the model has only eight nonequivalent Al sites in its unit cell, this is perhaps an indication a higher-order crystalline approximant is needed to obtain a simulated NQR spectrum which appears continuous.

One may estimate the minimum number of nonequivalent Al sites in Al-Cu-Fe and Al-Cu-Ru quasicrystals, based on reasonable assumptions about the intrinsic linewidths for each nonequivalent site. Two mechanisms contribute to the intrinsic NQR linewidths: dipolar broadening due to interactions between nearest neighbors of like and unlike nuclei, and quadrupolar broadening due to defects and strains. The dipolar linewidth, which is dominated by the ^{27}Al - ^{27}Al interaction, can be estimat-

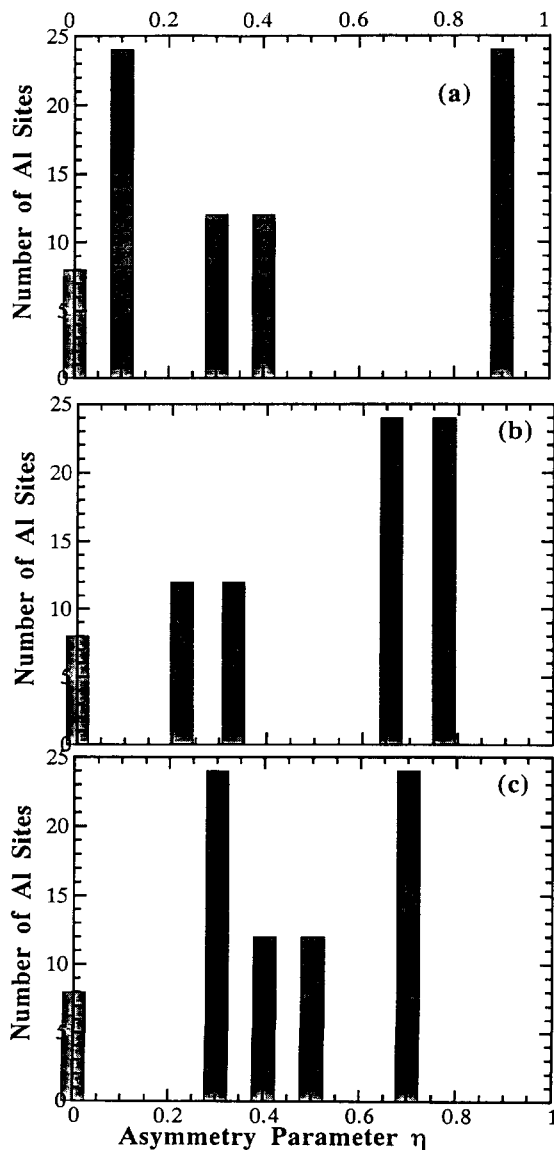


FIG. 11. Distribution of η for different net charges on the Al, Cu, and Ru(Fe) ions, respectively: (a) 3,1,1; (b) 3,1,2; (c) 3,1,3.

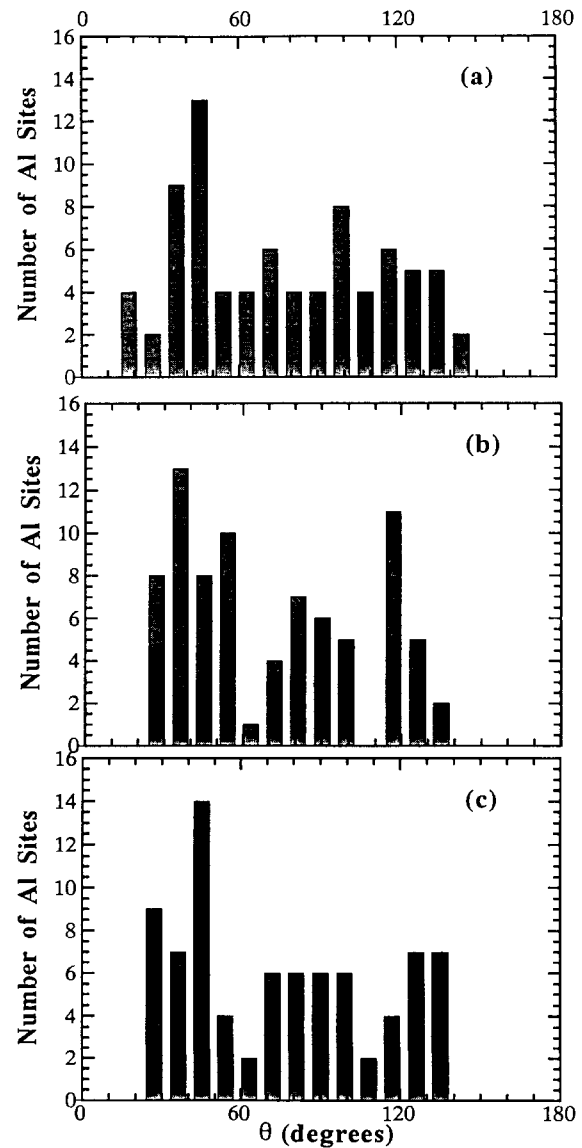


FIG. 12. Distribution of θ for different net charges on the Al, Cu, and Ru(Fe) ions, respectively: (a) 3,1,1; (b) 3,1,2; (c) 3,1,3. The bin width is 9° .

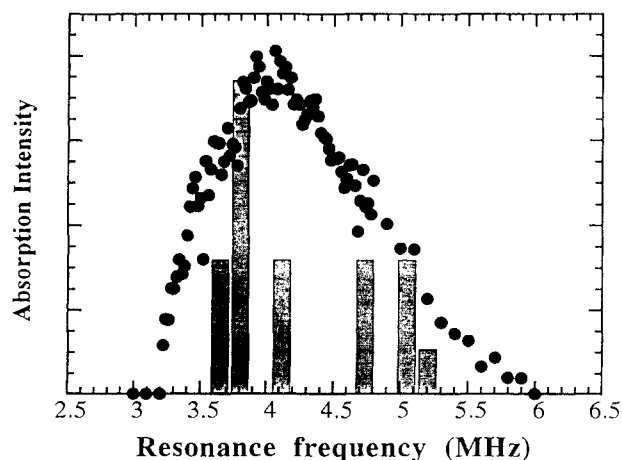


FIG. 13. Comparison of $|V_{zz}^{\text{latt}}|$ histogram for Al, Cu, and Fe(Ru) charges 3,1,1, based on Eq. (8), superimposed on the NQR spectrum for $\text{Al}_{70}\text{Cu}_{15}\text{Ru}_{15}$. The heights of the histogram bars were rescaled to get the maximum of the histogram to agree with the experimental value. The different η values for the nonequivalent sites have been taken into account.

ed to be $2\sigma \approx 2$ kHz, and is thus negligible.

The intrinsic linewidth due to strains and defects may be induced by quadrupolar broadening, and depends on the concentration of defects. Since the quality of our QC samples is quite good (see the x-ray spectra in Fig. 1) we may assume that the broadening due to defects is of the order of what is found in the ^{27}Al NQR spectra in LaAl_2 (Ref. 31) and $\text{Al}_3\text{Pd}_2\text{U}$,³² namely, 20 kHz. One source of extrinsic broadening may be the small applied field ($H_0 \approx 30$ G) needed to enhance the signal-to-noise ratio (see Sec. II D), which might conceivably broaden the lines 35 kHz. A generous upper limit for the width of each component of the NQR spectrum could then be reasonably set at 100 kHz.

To place a lower limit on the number of nonequivalent aluminum sites, the lack of any resolvable fine structure in the NQR spectra of Fig. 9 indicates that the intrinsic linewidth due to each nonequivalent aluminum site is larger than the difference in frequency between neighboring resonance lines. Though setting a criterion for the resolvability of the component NQR lines is somewhat arbitrary, we took as a reasonable upper limit for the average separation between component NQR resonances the values $\delta/2$, where δ is the FWHM of the intrinsic linewidth. Dividing the full frequency range of the distribution, Δ , by the separation between adjacent NQR resonance lines, one gets an estimate of the number of component resonance lines n , and therefore the number of nonequivalent sites: $n \geq \Delta/\delta/2$. For $\Delta = 2.5$ MHz from Fig. 9, and $\delta = 100$ kHz as discussed above, one gets $n \geq 50$ nonequivalent Al sites in the Al-Cu-Fe and Al-Cu-Ru quasicrystals.

We point out that this number does not necessarily require significant differences between the local Al environments in the 1/1 quasicrystalline approximant model employed and the quasicrystals studied, since the electric-field gradient from the atomic nearest-neighbor shells

varies relatively slowly with distance. Indeed, given the good agreement between the width of the NQR resonance and the distribution calculated for the approximant, it is likely the nearest-neighbor environments are quite similar. The range of nonequivalent local environments in the quasicrystal arises, then, from differences in the third, fourth, or perhaps more distant coordination shells. This implies the structure of the clusters used in the approximant could very well be the same as in the quasicrystal, but the arrangement of the clusters should be different for the quasicrystal. These differences can effectively broaden the discrete frequencies calculated for the approximant and "fill in" the gaps in the simulated spectrum (see Fig. 13).

E. ^{63}Cu NMR and local symmetry at the Cu site

As shown in Figs. 2 and 5 the $^{63,65}\text{Cu}$ NMR signals are superimposed on the broad background due to the ^{27}Al satellite resonances. This prevents an accurate study of the $^{63,65}\text{Cu}$ NMR linewidth and shape. However, some information about the local symmetry at the Cu site can be obtained by comparing the $^{63,65}\text{Cu}$ NMR with the ^{27}Al NMR. The observed $^{63,65}\text{Cu}$ NMR lines arise from the central-line transition ($+\frac{1}{2} \leftrightarrow -\frac{1}{2}$), while the satellite contribution is broadened beyond the limit of detection. Since both ^{63}Cu and ^{27}Al central lines are broadened by second-order quadrupole effects, the ratio of the corresponding widths should be

$$\frac{^{63}\Delta}{^{27}\Delta} = \frac{3}{8} \left[\frac{\overline{^{63}v_Q}}{\overline{^{27}v_Q}} \right]^2, \quad (10)$$

where $\overline{v_Q}$ is an average quadrupole coupling frequency, and the $\frac{3}{8}$ factor arises from the nuclear spins of Al and Cu.³⁷ From NMR data of Figs. 2 and 5, one finds $^{63}\Delta/^{27}\Delta \approx 3$ at 8.2 T, and $^{63}\Delta/^{27}\Delta \approx 2$ at 2.1 T. We considered this to be reasonably consistent with the field independence of Eq. (10), and attributed the discrepancy to difficulty in separating the Al and Cu central-line widths at 24 MHz. Taking the 8.2-T value $^{63}\Delta/^{27}\Delta \approx 3$ and $^{27}v_Q = 2.1$ MHz, one has

$$\overline{^{63}v_Q} \approx 3 \overline{^{27}v_Q} = 6.3 \text{ MHz}.$$

One may then compare the average electric-field gradients at the nuclear sites for Al and Cu, to determine if the chemical ordering of the quasilattice yields similar local environments for the two nuclei. The ratio of quadrupole coupling frequencies should be given by

$$\begin{aligned} \frac{\overline{^{63}v_Q}}{\overline{^{27}v_Q}} &= \frac{10}{3} \frac{^{63}Q}{^{27}Q} \frac{|\overline{^{63}V_{zz}^{\text{tot}}}|}{|\overline{^{27}V_{zz}^{\text{tot}}}|} \\ &= \frac{10}{3} \frac{^{63}Q}{^{27}Q} \frac{|\overline{^{63}V_{zz}^{\text{el}}}| - |\overline{^{63}V_{zz}^{\text{latt}}}|(1 - ^{63}\gamma_\infty)}{|\overline{^{27}V_{zz}^{\text{el}}}| - |\overline{^{27}V_{zz}^{\text{latt}}}|(1 - ^{27}\gamma_\infty)}. \end{aligned} \quad (11)$$

As mentioned previously, for many nuclei in a wide variety of metals and alloys, the ratio of the electronic to the lattice contributions of the total electric field gradient is about 2–4.³³ By defining $r \equiv |\overline{V_{zz}^{\text{el}}}|/|\overline{V_{zz}^{\text{latt}}}|(1 - \gamma_\infty)$, we

rewrite Eq. (11) as

$$\frac{\overline{63\nu_Q}}{\overline{27\nu_Q}} = \frac{10}{3} \frac{63Q}{27Q} \frac{(1-63\gamma_\infty)}{(1-27\gamma_\infty)} \frac{|\overline{63V_{zz}^{\text{latt}}|}}{|\overline{27V_{zz}^{\text{latt}}|}} \frac{(63r-1)}{(27r-1)}. \quad (12)$$

Before deriving any conclusions from the comparison of theory and experiments, we want to be sure that the copper NMR signal measured is representative of all copper nuclei in the sample, and not of merely a small fraction.

To do this, we studied the areas under the copper and aluminum central lines at 24 MHz. The areas under the central lines, denoted by A , can be related to the number of nuclei by

$$\frac{63A + 65A}{27A} = \frac{\frac{2}{3}(63\gamma)^3 + \frac{1}{3}(65\gamma)^3}{(27\gamma)^3} \times \frac{\frac{3}{2}(\frac{3}{2}+1)}{\frac{5}{2}(\frac{5}{2}+1)} \frac{0.40}{0.26} \frac{\text{Cu}N}{\text{Al}N}, \quad (13)$$

where N is the total number of copper or aluminum nuclei. For the alloys $\text{Al}_{85-x}\text{Cu}_x\text{Ru}_{15}$ ($x=15, 17, 20$) and $\text{Al}_{65}\text{Cu}_{23}\text{Fe}_{12}$, Eq. (13) gives theoretical values of

$$\left(\frac{\text{Cu}A}{\text{Al}A} \right)_{\text{theory}} \equiv \frac{63A + 65A}{27A} \approx 0.15 - 0.21, 0.24,$$

respectively. To determine the experimental integrated lines intensities $27A$, $63A$, and $65A$, we measured the areas beneath the central lines and above the Al satellite background in all field-scan spectra at 24 MHz. For both the Al-Cu-Ru and Al-Cu-Fe systems we obtained

$$\left(\frac{\text{Cu}A}{\text{Al}A} \right)_{\text{expt}} \equiv \frac{63A + 65A}{27A} \approx 0.15 \pm 0.04.$$

The resulting agreement between theory and experiment indicates that most of the copper nuclei do contribute to the observed NMR signal.

To compare the result of Eq. (12) with experiment, we performed a simulation of $|V_{zz}^{\text{latt}}|$ at the copper sites in the Al-Cu-Fe 1/1 approximant model discussed previously, to determine the distribution of gradients. The simulation was performed as described earlier for aluminum NQR, but for the copper sites. Figure 14 gives the $|V_{zz}^{\text{latt}}|$ histograms for three charge configurations of Fe(Ru), and one finds the mean values of the aluminum (from data of Fig. 10) and copper lattice gradients to be such that $|\overline{63V_{zz}^{\text{latt}}}| \approx 0.8|\overline{27V_{zz}^{\text{latt}}}|$. Therefore, in order to obtain the experimental value of 3 for the ratio $\overline{63\nu_Q}/\overline{27\nu_Q}$ in Eq. (12), one has to assume $(63r-1) = 0.16(27r-1)$, where we used the values $27Q = 0.140 \times 10^{-24} \text{ cm}^2$, $63Q = 0.209 \times 10^{-24} \text{ cm}^2$, $(1-27\gamma_\infty) = 3.3$, $(1-63\gamma_\infty) = 16$, and $|\overline{63V_{zz}^{\text{latt}}}| \approx 0.8|\overline{27V_{zz}^{\text{latt}}}|$. Since we found $27r \approx 5$ from the analysis of the 27Al NQR spectrum, one deduces $63r \approx 1.6$. Even allowing for large uncertainties in this derivation, due mostly to the assumed values of the antishielding factor $(1-\gamma_\infty)$, one can conclude that the electronic part of the EFG, $|V_{zz}^{\text{el}}|$, at the Cu site is smaller (by a factor of 2–3) than the corresponding value at the

Al site. This conclusion is consistent with a more s -like character of the conduction-electron wave function at the Cu site than at the Al site. In addition, from the above analysis we inferred ν_Q for 63Cu should be around 6 MHz. It would be interesting to search for the 63Cu NQR signal around 6 MHz, although the spectrum is expected to be even broader than the 27Al spectrum in Fig. 9, and therefore difficult to detect.

IV. KNIGHT SHIFT, SPIN-LATTICE RELAXATION, AND ELECTRONIC PROPERTIES

A. Knight shift

The experimental measurement of the Knight shift was made uncertain because the spectrum was broadened by a

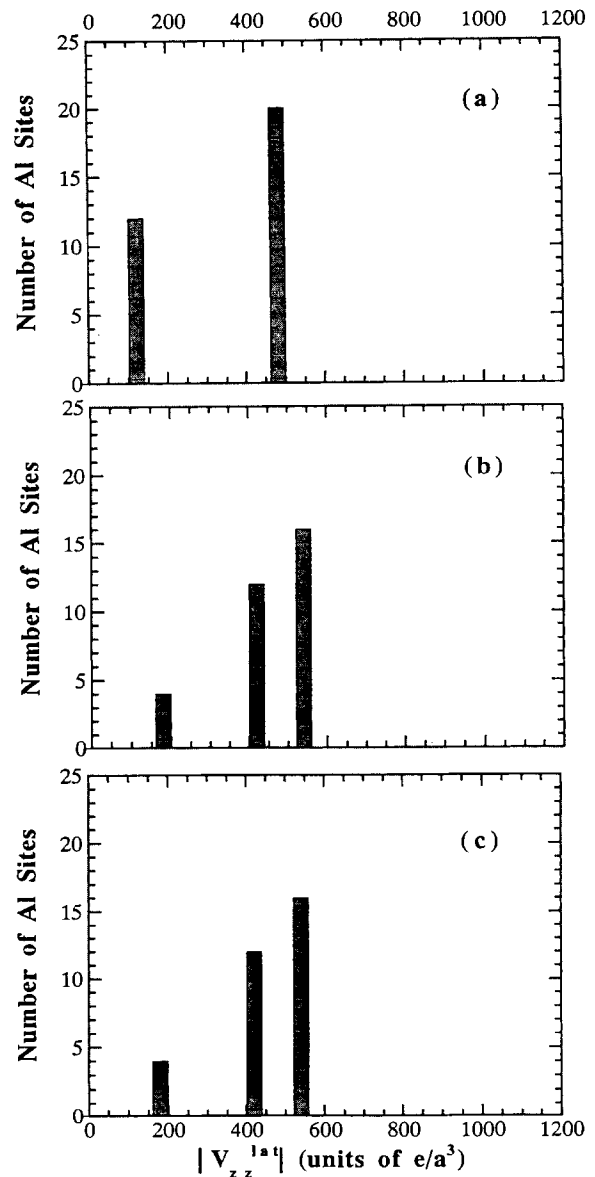


FIG. 14. Distribution of $|V_{zz}|$ for the copper sites, in units of e/a^3 , for different net charges on the Al, Cu, and Ru(Fe) ions, respectively: (a) 3,1,1; (b) 3,1,2; (c) 3,1,3. The bin width is $60e/a^3$.

distribution of quadrupole interactions, as discussed in the previous section. From the simulation of the NMR lines one can deduce a value for the isotropic Knight shift K_{iso} (see Table I). This is possible because the isotropic part of the Knight-shift tensor produces a shift of the entire NMR spectrum without contributing to the width. The anisotropic shift K_{an} contributes mainly to the broadening. In the presence of both quadrupole and anisotropic Knight-shift interactions one expects the linewidth has a magnetic contribution proportional to the resonance frequency ν_R and a quadrupole contribution proportional to $1/\nu_R$.³⁸

$$\Delta = \frac{a}{\nu_R} + b\nu_R, \quad (14)$$

where the exact values of the constants a and b will depend upon the distribution of both the quadrupole coupling constants and the Knight-shift tensor components. The intrinsic dipolar width of the line is assumed to be negligible. Equation (14) does not assume any particular symmetry for the nuclear sites. The experimental results are shown in Fig. 15 in a plot of Δ/ν_R vs $1/\nu_R^2$. Although only three points are available for each sample one can see that the behavior predicted by Eq. (14) is in agreement with the experimental points. In particular, the slope a of the line—which should be proportional to $(\overline{\nu_Q})^2$ —scales as expected with the average ν_Q values obtained from the simulation of the spectra (see Table I). The infinite-frequency intercept, b , is nearly zero, leading to the conclusion that the anisotropic part of the Knight-shift tensor is negligibly small.

B. Spin-lattice relaxation rates

As discussed in Sec. II D, the recovery of the nuclear magnetization can be fitted by Eqs. (1) and (2), indicating that the spin-lattice relaxation mechanism is dominated by magnetic rather than quadrupolar interactions. The relaxation transition probabilities are summarized in Table II for two temperatures. Furthermore, the temperature dependence of W_m for ^{27}Al is shown in Fig. 16. As discussed previously,⁹ the data show no measurable dependence of W_m on the composition of the alloy [Fig. 16(a)] or on the long-range order [Fig. 16(b)]. In all cases the temperature dependence of W_m for ^{27}Al is linear up

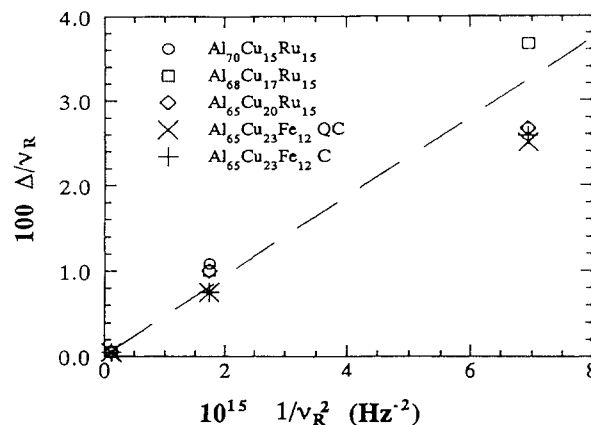


FIG. 15. Δ/ν_R vs $1/\nu_R^2$ for ^{27}Al in Al-Cu-Ru and Al-Cu-Fe systems.

to liquid-nitrogen temperature as expected for a relaxation mechanism due to conduction electrons. The parameter $2W_m$ in Eqs. (1) and (2) was used as T_1^{-1} , the spin-lattice relaxation time, in the Korringa relation. The best estimates of the ^{27}Al Korringa product, $(T_1 T)^{-1}$, obtained from fitting the data in Fig. 16 are 0.0065 ± 0.0006 , 0.0052 ± 0.0003 , and $0.0055 \pm 0.0003 \text{ s}^{-1} \text{ K}^{-1}$ in Al-Cu-Ru for $x=15$, 17, and 20; and 0.0052 ± 0.003 and $0.0049 \pm 0.0003 \text{ s}^{-1} \text{ K}^{-1}$ in Al-Cu-Fe C and QC, respectively.

Considering the $^{63,65}\text{Cu}$ NSLR, the data are insufficient to draw a firm conclusion about the relaxation mechanism. The values of W_m shown in Table II seem to indicate an increase of W_m with temperature faster than linear—which is similar to the behavior of a system with a quadrupole contribution to the relaxation rate.³⁹ The ratio of the NSLR for the two isotopes, also shown in Table II, is also intermediate between the values expected for magnetic relaxation, where the ratio should be $(^{63}\gamma/^{65}\gamma)^2=0.87$, and quadrupole relaxation, in which case it should be $(^{63}Q/^{65}Q)^2=1.14$.

C. NMR, magnetic susceptibility, and electronic structure

The magnetic susceptibility was measured as a function of temperature in the three Al-Cu-Ru quasicrystals. The total susceptibility is diamagnetic with a small Curie term

TABLE II. Nuclear spin-lattice relaxation rates.

	Sample ^a	$^{27}W_m$ (Hz)	$^{63}W_m$ (Hz)	$^{65}W_m$ (Hz)	$^{63}W_m/^{65}W_m$
77 K	15	0.25 ± 0.02	0.51 ± 0.02	0.52 ± 0.02	0.97 ± 0.08
	17	0.20 ± 0.01	0.45 ± 0.02	0.42 ± 0.01	1.08 ± 0.07
	20	0.21 ± 0.01	0.46 ± 0.02	0.46 ± 0.01	1.00 ± 0.07
	C	0.20 ± 0.01	0.34 ± 0.02	0.40 ± 0.02	0.86 ± 0.09
	QC	0.19 ± 0.01	0.46 ± 0.02	0.43 ± 0.01	1.07 ± 0.07
300 K	15	1.57 ± 0.05	4.0 ± 0.2	4.8 ± 0.3	0.84 ± 0.09
	17	1.59 ± 0.04	3.7 ± 0.2	4.4 ± 0.3	0.84 ± 0.09
	20	1.38 ± 0.04	3.8 ± 0.2	5.0 ± 0.4	0.8 ± 0.1
	C	0.94 ± 0.04	3.0 ± 0.2	3.9 ± 0.2	0.8 ± 0.1
	QC	0.70 ± 0.04	2.3 ± 0.1	2.4 ± 0.1	0.95 ± 0.06

^aNumber refers to x for $\text{Al}_{85-x}\text{Cu}_x\text{Ru}_{15}$; C and QC refer to phases of $\text{Al}_{65}\text{Cu}_{23}\text{Fe}_{12}$.

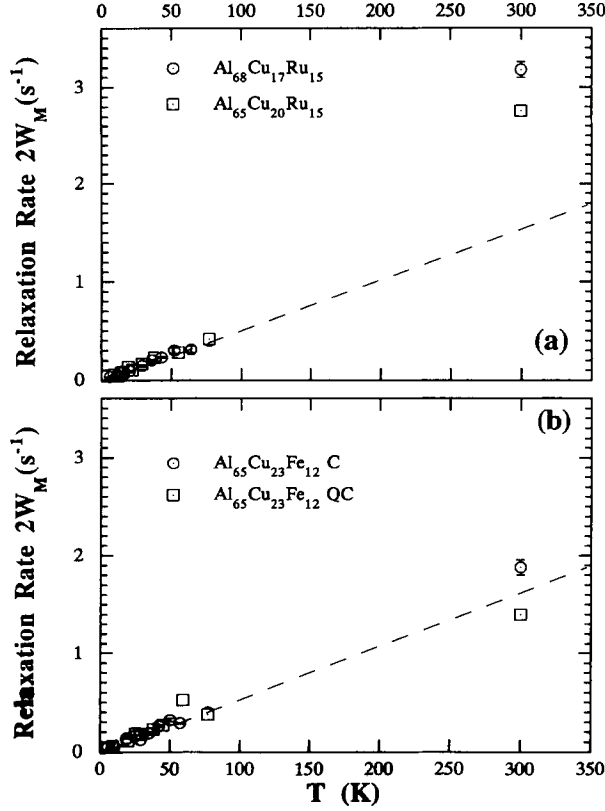


FIG. 16. ^{27}Al nuclear spin-lattice relaxation rates vs temperature for (a) Al-Cu-Ru system for $x = 17, 20$; (b) Al-Cu-Fe system for C and QC phases.

consistent with a level of paramagnetic impurity less than 0.01 at. % as expected from the 99.99% purity of the elemental constituents of the samples. The values of the temperature-independent term χ_0 , obtained after subtracting the Curie term, are shown in Table III. Also shown in Table III are the values of the Pauli susceptibility obtained from the expression³⁷

$$\chi_p = \frac{3}{2}(\chi_0 - \chi_{\text{dia}}). \quad (15)$$

The diamagnetic core contribution was estimated from the weighted sum of the theoretical values calculated by relativistic Hartree-Fock methods,³⁷ assuming nonionized atomic configurations consistent with the very low density of conduction-electron states in these materials.

The results for χ_p are highly approximate in view of the fact that their values depend entirely upon the theoretical estimate of the diamagnetic term. However, the relative values for the three different contributions of the alloys are determined by the experimental error on

TABLE III. Temperature-independent, diamagnetic, and Pauli susceptibility.

x	$10^6\chi_0$ (emu/mol)	$10^6\chi_{\text{dia}}$ (emu/mol)	$10^6\chi_p$ (emu/mol)
15	-24	-28	5
17	-24	-28	5
20	-24	-28	5

the susceptibility measurements. An analysis of the results for χ_p and for the ^{27}Al NMR parameters $(T_1 T)^{-1}$ and K_{iso} in Al-Cu-Ru quasicrystals gives useful information about the electronic structure. The most meaningful way to analyze the data turns out to be a comparison of the data for QC's and pure Al metal. The value of χ_p for Al metal is 30×10^{-6} emu/mol, which is about six times larger than the value for Al-Cu-Ru QC's (see Table III). The Knight shift for Al metal is $K_{\text{iso}} = 0.16\%$, which is about seven times larger than in Al-Cu-Ru QC's. Finally, $(T_1 T)^{-1} = 0.54 \text{ s}^{-1} \text{ K}^{-1}$ for Al metal which is about 100 times larger than in Al-Cu-Ru QC's (see previous section). One may interpret the data based upon the following equations, which show how each parameter depends upon either the *total* electronic density of states (DOS) at the Fermi energy $D(E_F)$ —as in the case of χ_p —or the *s*- and *d*-band DOS $D_s(E_F), D_d(E_F)$ —as in the case of K_{iso} and $(T_1 T)^{-1}$:⁴⁰

$$\begin{aligned} \chi_p &\propto D(E_F), \\ K_{\text{iso}} &= \mu_B D_s(E_F) H_s^{\text{hf}} + \mu_B D_d(E_F) H_d^{\text{hf}} + \chi_{\text{VV}} H_{\text{orb}}^{\text{hf}} / \mu_B, \\ (T_1 T)^{-1} &= \alpha_s K_s^2 + \alpha_d K_d^2 + \alpha_{\text{orb}} [\mu_B D_d(E_F) H_{\text{orb}}^{\text{hf}}]^2. \end{aligned} \quad (16)$$

The quantities $H_{s,d,\text{orb}}^{\text{hf}}$ are the magnetic hyperfine fields at the nucleus due, respectively, to the *s*- and *d*-band electrons, and to the electronic orbit; χ_{VV} is the Van Vleck susceptibility; and $\alpha_{s,d,\text{orb}}$ are prefactors of the *s*, *d*, and orbital terms. In Al metal the main contributions to both K_{iso} and $(T_1 T)^{-1}$ comes from *s*-band electrons. Because all three quantities in Eq. (16) scale by a factor of about 7 with respect to Al metal, the symmetry of the conduction-electron wave function at the Al site is similar in Al metal and in Al-Cu-Ru QC's and indicates the total density of states is reduced by almost one order of magnitude. This is in agreement with the formation of a pseudogap at the Fermi energy.

A comparison with specific-heat data for the electronic contribution γ which is also proportional to the total density of states is in order. Data published for $\text{Al}_{85-x}\text{Cu}_x\text{Ru}_{15}$ QC alloys are⁴¹ 1.1×10^3 , 2.3×10^3 , and $2.0 \times 10^3 \text{ erg}(\text{g-at. K}^2)^{-1}$ for $x = 20, 17$, and 15 , respectively. With the exception of the value for $x = 20$, the ratios of the γ values for Al-Cu-Ru QC's to $\gamma = 13.6 \times 10^3 \text{ erg g-at.}^{-1}$ for pure Al metal again yields a factor close to 7, consistent with the scalings of the NMR parameters and the Pauli susceptibility. The smaller value of γ found for $x = 20$ led to the suggestion of the presence of distinct features in the DOS in the narrow region of *I*-phase formation. Our data are not consistent with fine structure in the DOS. On the contrary, the pseudogap at the Fermi surface seems to be rather insensitive to both the details of the structure and the composition of the alloy.

V. SUMMARY AND CONCLUSIONS

^{27}Al NMR spectra in the Al-Cu-Ru and Al-Cu-Fe quasicrystalline and crystalline approximant phases give clear evidence for a quasicontinuous distribution of

electric-field gradient tensor components at the aluminum sites. The quadrupole-perturbed NMR spectra were analyzed with a line-shape simulation program, and we found a Gaussian distribution of quadrupole coupling constants gave satisfactory agreement with the experimental data.

Guided by the quadrupole interaction strengths inferred from the NMR spectra, we were able to observe the ^{27}Al NQR spectrum at 4.2 K. The NMR and NQR data were found to be in good agreement, and both unambiguously indicated the existence of a very wide distribution of quadrupole interactions at the aluminum sites. A model calculation of the aluminum electric-field gradients in Al-Cu-Ru was successful in explaining the observed quadrupole interactions. The agreement between the ^{27}Al NQR spectral data and the simulations indicated that the average EFG value was largely determined by the Al atomic p wave function, and was approximately the same for all Al sites. Additionally, we concluded that the EFG distribution in the Al-Cu-Fe and Al-Cu-Ru quasicrystals around the average EFG value comes mainly from the ionic lattice contribution, and in this respect quasicrystals are more like covalent crystals than metals. In particular, we concluded that the unusually wide distribution of quadrupole resonance frequencies in the NQR spectrum may be explained by a multiplicity of nonequivalent aluminum sites within the quasilattice. We obtained a lower limit of approximately 50 nonequivalent aluminum sites, based on a reasonable value for the width of each NQR component of the spectrum due to lattice defects and strains.

In addition, the ^{27}Al NMR line in a single-grain Al-Pd-Mn quasicrystal was the same within experimental uncertainty for several orientations of the sample with respect to the magnetic-field direction, leading us to conclude there must be a wide distribution of EFG PAS

orientations in the QC.

^{63}Cu NMR was less conclusive, but indicated that the average experimental EFG at the copper sites is significantly less than the average EFG at the aluminum sites. Since the calculation of the lattice contribution to the EFG yields comparable results at the aluminum and copper sites, we tentatively concluded the difference observed should be ascribed to a more s -like symmetry of the valence electronic wave function at the copper sites with respect to the aluminum sites.

The values of the ^{27}Al Knight shift, relaxation time, and bulk magnetic susceptibility measurements confirm the existence of a pseudogap in the electronic density of states in both Al-Cu-Fe and Al-Cu-Ru, consistent with the large overlap of the highly symmetric pseudo-Brillouin-zone boundary and the Fermi surface. In Al-Cu-Fe, the 3/2 approximant phase had Knight-shift and relaxation-time measurements which were the same as those for the quasicrystal, within experimental uncertainty. This is consistent with the view that the electronic properties are determined by short- and intermediate-range, rather than long-range, order. In Al-Cu-Ru, no dependence of Knight shift or relaxation rate on copper concentration occurred within experimental uncertainty. We conclude that, on an energy scale of ≈ 0.02 eV, the s -band density of states in Al-Cu-Ru shows no unusually rapid variations of the kind previously proposed to account for specific-heat and thermopower data in the Al-Cu-Ru system.

ACKNOWLEDGMENTS

The authors thank S. W. Kycia, T. A. Lograsso, and D. W. Delaney for the Al-Pd-Mn sample. Ames Laboratory is operated for the U.S. Department of Energy by Iowa State University under Contract No. W-7405-Eng-82.

*Also at Dipartimento di Fisica, Università di Pavia, 27100 Pavia, Italy.

†Present address: Department of Materials Science and Engineering, University of Utah, Salt Lake City, UT 84112.

¹A. I. Goodman and M. Widom, *Annu. Rev. Phys. Chem.* **42**, 685 (1991).

²S. J. Poon, *Adv. Phys.* **41**, 303 (1992).

³W. W. Warren, H. S. Chen, and J. S. Hauser, *Phys. Rev. B* **32**, 7614 (1985).

⁴M. Rubinstein and G. H. Stauss, *J. Mater. Res.* **1**, 243 (1986).

⁵K. R. Carduner, B. H. Suits, J. A. DiVerdi, M. D. Murphy, and D. White, *J. Mater. Res.* **2**, 431 (1987).

⁶C. Lee, D. White, B. H. Suits, P. A. Bancel, and P. A. Heiney, *Phys. Rev. B* **37**, 9053 (1988).

⁷E. Jeong, J. C. Holzer, A. E. Carlsson, M. S. Conradi, P. A. Fedders, and K. F. Kelton, *Phys. Rev. B* **41**, 1695 (1990).

⁸A. R. Drews, M. Rubinstein, G. H. Stauss, L. H. Bennet, and L. J. Swartzendruber, *J. Alloys Compounds* **190**, 189 (1993).

⁹A. Shastri, F. Borsa, A. I. Goldman, J. E. Shield, and D. R. Torgeson, *J. Non-Cryst. Solids* **153&154**, 347 (1993).

¹⁰H. Yasuoka, A. Soyama, K. Kimura, and S. Takeuchi, *J. Phys. Soc. Jpn.* **55**, 1058 (1986).

¹¹F. Hippert, L. Kandel, Y. Calvayrac, and B. Dubost, *Phys. Rev. Lett.* **69**, 2086 (1992).

¹²T. Shinohara, A. P. Tsai, and T. Masumoto, *J. Mater. Res.* **7**, 62 (1992).

¹³H. Fujimaki, K. Motoya, H. Yasuoka, K. Kimura, T. Shibuya, and S. Takeuchi, *J. Phys. Soc. Jpn.* **60**, 2067 (1991).

¹⁴E. Hill, T. C. Chang, Y. Wu, S. J. Poon, F. S. Pierce, and Z. M. Stadnik, *Phys. Rev. B* **49**, 8615 (1994).

¹⁵A. Shastri, Ph.D. dissertation, Iowa State University, 1994.

¹⁶A. I. Goldman, J. E. Shield, C. A. Guryan, and P. W. Stephens, in *Proceedings of the 25th Anniversary Adriatico Research Conference on Quasicrystals*, edited by M. Jaric and S. Lundqvist (World Scientific, Singapore, 1990), p. 60.

¹⁷M. Audier and P. Guyot, *Proceedings of the 25th Anniversary Adriatico Research Conference on Quasicrystals* (Ref. 16), p. 74.

¹⁸P. Bancel, *Phys. Rev. Lett.* **63**, 496 (1990).

¹⁹J. M. Dubois, C. Dong, C. Jonot, M. de Boissieu, and M. Audier, *Phase Transitions* **32**, 3 (1991).

²⁰S. W. Kycia, A. I. Goldman, T. A. Lograsso, D. W. Delaney, D. Black, M. Sutton, E. Dufresne, R. Bruening, and B. Rodricks, *Phys. Rev. B* **48**, 3544 (1993).

- ²¹The NMR spectrometer employed a programmable pulse sequencer [D. J. Adduci and B. C. Gerstein, *Rev. Sci. Instrum.* **50**, 1403 (1979)]; a double-sideband rf switch [D. R. Torgeson and D. J. Adduci (unpublished)]; and a receiver similar to D. J. Adduci, P. A. Hornung, and D. R. Torgeson, *Rev. Sci. Instrum.* **47**, 1503 (1976), with quadrature detector [Dr. R. Torgeson (unpublished)].
- ²²C. P. Slichter, *Principles of Magnetic Resonance* (Springer-Verlag, New York, 1990).
- ²³H. Chihara and N. Nakamura, in *Crystal and Solid Physics*, edited by K. H. Hellwege and A. M. Hellwege, Landolt-Börnstein, New Series, Group III, Vol. 20, Pt. a (Springer-Verlag, Berlin, 1988), pp. 2–37.
- ²⁴C. Dimitropoulos, M. Maglione, and F. Borsa, *Phys. Rev. B* **37**, 3159 (1988).
- ²⁵A. Narath, *Phys. Rev.* **162**, 320 (1967).
- ²⁶E. R. Andrew and D. P. Tunstall, *Proc. Phys. Soc. London* **78**, 1 (1961).
- ²⁷P. C. Taylor and P. J. Bray, *J. Magn. Reson.* **2**, 305 (1970); P. C. Taylor, J. F. Baugher, and H. M. Kriz, *Chem. Rev.* **75**, 203 (1975).
- ²⁸R. R. Hewitt and T. T. Taylor, *Phys. Rev. B* **125**, 524 (1962).
- ²⁹K. Ishida *et al.*, *J. Phys. Soc. Jpn.* **62**, 2803 (1993).
- ³⁰Z. Tan *et al.*, *Physica C* **156**, 137 (1988).
- ³¹D. E. MacLaughlin and M. Daugherty, *Phys. Rev. B* **6**, 2502 (1972).
- ³²M. Kyogaku, Y. Kitaoka, K. Asayama, C. Geibel, C. Schank, and F. Steglich, *J. Phys. Soc. Jpn.* **62**, 4016 (1993).
- ³³E. N. Kaufmann and R. J. Vianden, *Rev. Mod. Phys.* **51**, 161 (1979).
- ³⁴R. S. Raghavan, E. N. Kaufmann, and P. Raghavan, *Phys. Rev. Lett.* **34**, 1280 (1975).
- ³⁵M. H. Cohen and R. Reif, in *Solid State Physics: Advances in Research and Applications*, edited by F. Seitz and D. Turnbull (Academic, New York, 1957), Vol. 5, p. 321.
- ³⁶E. Cockayne *et al.*, *J. Non-Cryst. Solids* **153&154**, 140 (1993).
- ³⁷G. C. Carter, L. H. Bennet, and D. J. Kahan, *Metallic Shifts in NMR* (Pergamon, Oxford, 1977).
- ³⁸W. H. Jones, T. P. Graham, and R. G. Barnes, *Phys. Rev.* **132**, 1898 (1963).
- ³⁹A. Abragam, *Principles of Nuclear Magnetism* (Clarendon, Oxford, 1989).
- ⁴⁰Y. Yafet and V. Jaccarino, *Phys. Rev.* **133**, A1630 (1964).
- ⁴¹B. D. Biggs, S. J. Poon, and N. R. Munirathnam, *Phys. Rev. Lett.* **65**, 2700 (1990).

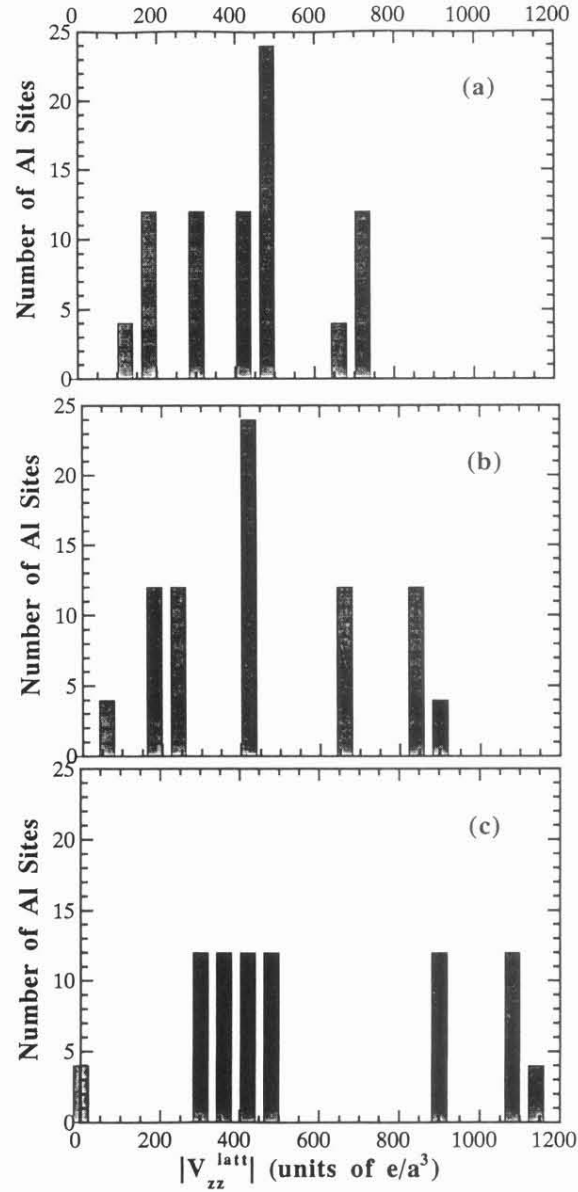


FIG. 10. Distribution of $|V_{zz}|$ EFG values for the aluminum sites, in units of e/a^3 , for different net charges on the Al, Cu, and Ru(Fe) ions, respectively: (a) 3,1,1; (b) 3,1,2; (c) 3,1,3. The bin width is $60e/a^3$.

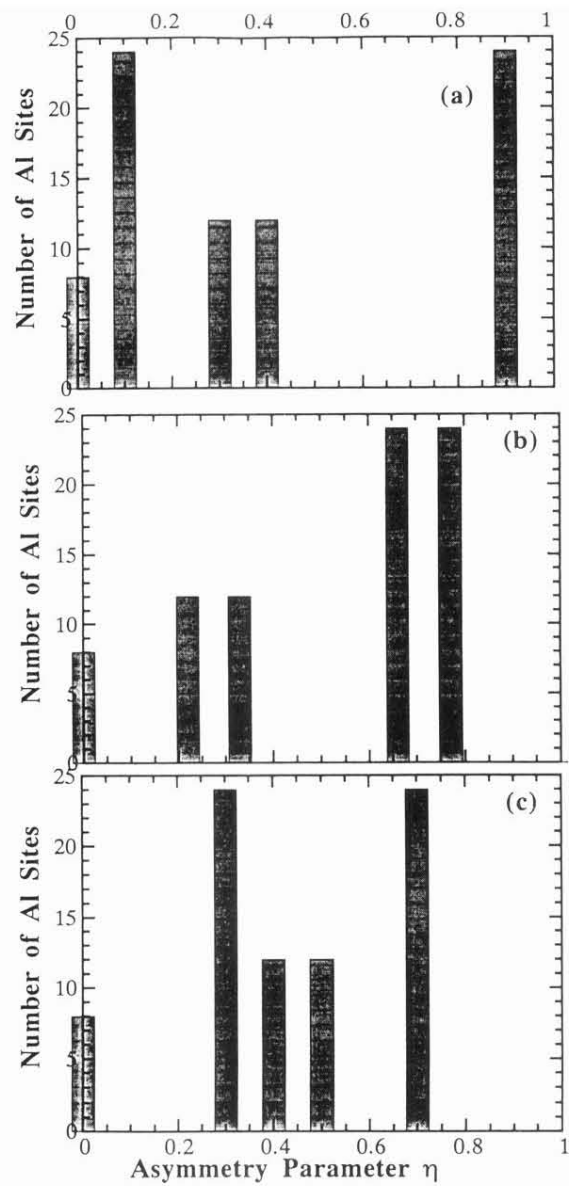


FIG. 11. Distribution of η for different net charges on the Al, Cu, and Ru(Fe) ions, respectively: (a) 3,1,1; (b) 3,1,2; (c) 3,1,3.

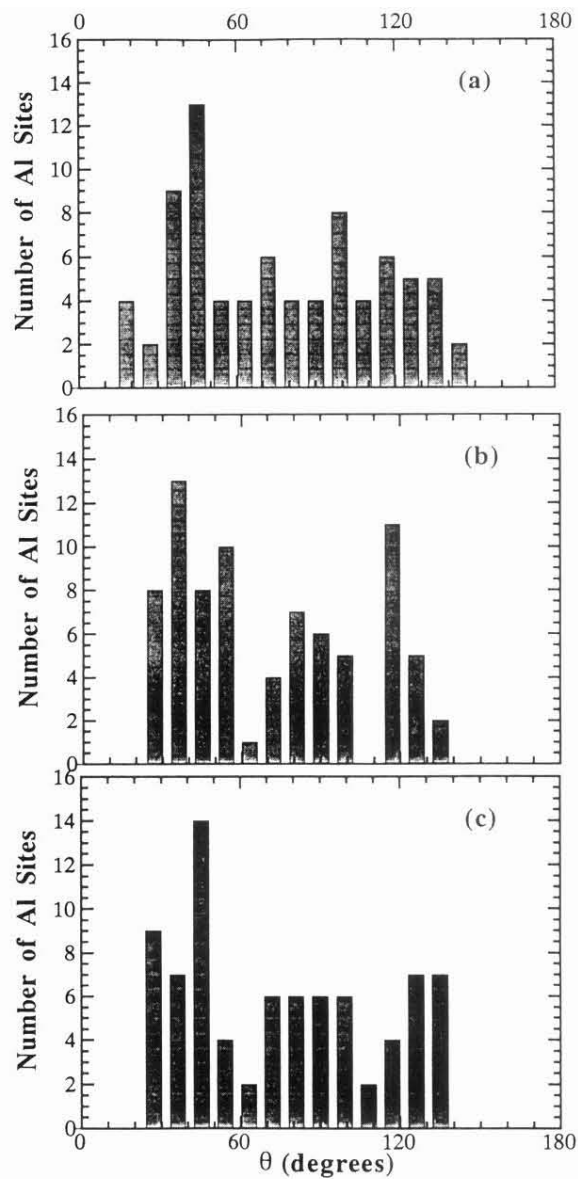


FIG. 12. Distribution of θ for different net charges on the Al, Cu, and Ru(Fe) ions, respectively: (a) 3,1,1; (b) 3,1,2; (c) 3,1,3. The bin width is 9° .

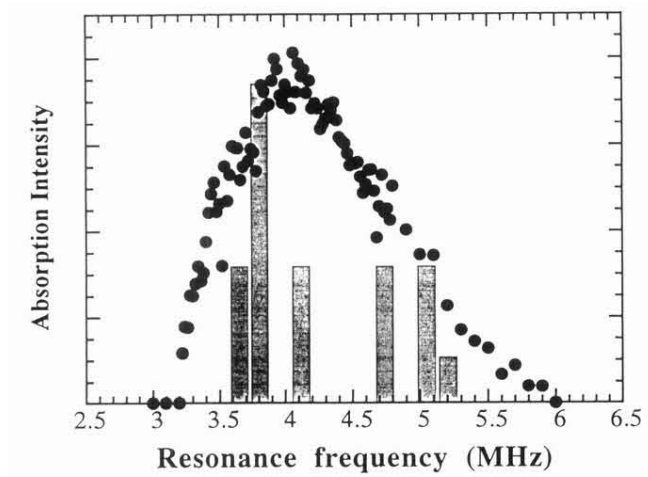


FIG. 13. Comparison of $|V_{zz}^{\text{latt}}|$ histogram for Al, Cu, and Fe(Ru) charges 3,1,1, based on Eq. (8), superimposed on the NQR spectrum for $\text{Al}_{70}\text{Cu}_{15}\text{Ru}_{15}$. The heights of the histogram bars were rescaled to get the maximum of the histogram to agree with the experimental value. The different η values for the nonequivalent sites have been taken into account.

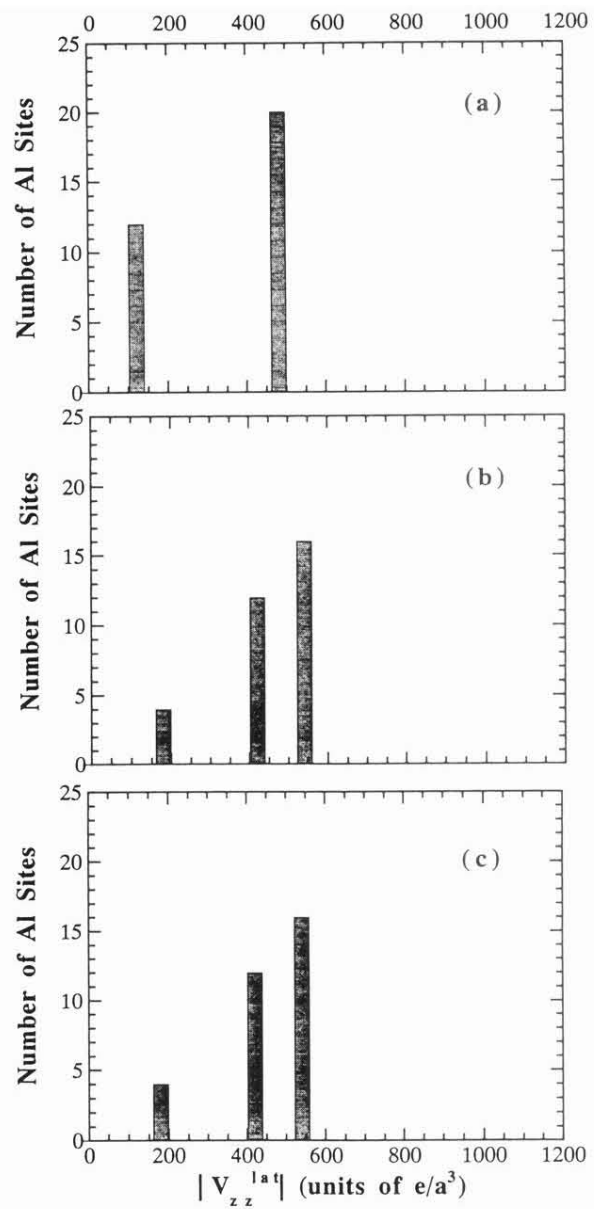


FIG. 14. Distribution of $|V_{zz}|$ for the copper sites, in units of e/a^3 , for different net charges on the Al, Cu, and Ru(Fe) ions, respectively: (a) 3,1,1; (b) 3,1,2; (c) 3,1,3. The bin width is $60e/a^3$.